Doctoral Dissertation

Title

Local-heterogeneous responses and transient dynamics in colloidal fluids

(コロイド流体における局所的な不均一応答と動態)

by

Preetom Nag

Graduate School of Life Science, Hokkaido Universiy

2014, December

For my wife "Nandita" and my little prince "Punit"

Acknowledgements

I would like to express my deepest gratitude to my advisor Professor Tamiki Komatsuzaki. I thank him for excellent guidance, caring, patience, and providing me with excellent atmosphere for doing research. His positive influence on my professional and personal devolopment will continue to benefit me throughout life.

I thank the other faculty members I have had the pleasure of interacting with. Specially, much of this thesis would not have been accomplished without the patient mentorship of assistant professor Hiroshi Teramoto. He introduced me several concepts on which this thesis is based and has played a crucial role in the development of the results.

I would also like to express my sincere gratitude to associate professor Chun Biu Li for his interesting conversations, mentoring and constructive feedback regarding my work. His remarkable creativity and intense dedication to research has been a source of inspiration to me, as well as so many other young scientists.

This thesis employs a colloidal system as an application of our analysis. I sincerely thank Professor Norbert F. Scherer for providing us sets of data for our analysis. I also thank lecturer Dr. Mitchio Otsuki for his valuable comments and suggestions at some part of our analysis.

I sincerely thank my co-supervisors Professor Naoki Sasaki and Professor Hisashi Haga for their valuable comments and suggestions to improve in writing some sections of this thesis.

In my daily work I have been blessed with a friendly and cheerful group of fellow lab members. At first I would like to thank Dr. Tahmina Sultana, who was very kind and helpful as an elder sister in my daily life of my PhD research. I thank Mr. Yutaka Nagahata, Mr. Naoki Miyagawa, Dr. Nick Taylor and others for their valuable comments and discussions in our meetings. I also thank other doctoral and master students for their helping attitude everytime whenever I needed them essentially.

I thank my family for encouraging me to follow my dream to become a scientist. I thank my younger sisters Purni and Puja for their deepest love and admiration. Without mentioning one name, my grandfather Hari Bhushan Majumder, I would not be at the position where I am now. I thank him for his love and supports, and for filling my childhood with happiness during all of the time we spent together. I thank my uncle Monoj Kumar Majumder for his love, inspiration to my study, for teaching me to stay positive and appreciate each day.

Most of all, I thank my parents for giving birth to me and supporting me spiritually throughout my life. I thank my mom for always emphasizing me the importance of education, all the little things that she has done (and continues to do) for me to make my life easier and happier. I thank both of my parents for their unwavering love and supports.

Words fail to express my appreciation to my wife Nandita whose dedication, love, understanding and persistent confidence in me, has taken the load off my shoulder from the time we met. She was always there cheering me up and stood by me through the good times and bad times. She has given me an wonderful, priceless gift in the world, my son "Punit". Her supports and encouragements were in the end what made this dissertation possible. I would also thank Shyam Sundar Banik's family for letting me take her hand in marriage, and accepting me as a member of the family warmly.

At the end, I would like to thank everybody who was important to the successful realization of this thesis, as well as expressing my apology that I could not mention personally one by one. Above all, I owe it all to Almighty God for granting me the wisdom, health and strength to undertake this research task and enabling me to its completion.

Abstract

All living organisms are composed of basic structural, functional, and biological unit such as cell. In biology, cell movement is one of the basic components to determine the phenotype. The motility of cells is a highly dynamic phenomenon that is essential to a variety of biological processes such as the embryonic development, wound healing, immune response and the cancer metastasis. For example, in wound healing in animals, white blood cells and macrophages move to the wound site to kill the microorganisms that cause infection. In most of the case, cells reach their target by crawling and sometimes they are found to move collectively. This collective motion indeed refers the heterogeneity in space and time of cells' motility in a living organism.

For example, a confluent epithelial cell sheet exhibits a collective migration and subcellular motion but, depending on the presence of their neighbors. Some cells undergo collective migration but the other cells are transiently disordered and immobile. As cell density increases, the number of cells migrating collectively increase up to some value of cell density. Dynamic characteristics of individual cells do not necessarily preserve, that is, some migrating cells turn to be immobile and immobile cells turn to be collectively mobile, depending on the local environment. However, in terms of the observed massive data flow, how to quantify such dynamic heterogeneity and how to extract the underlying dynamic structure that dominates the spatio-temporal dynamics of cells are one of the unresolved intriguing subjects. Along this aspect there exists a very similar phenomena observed in a system composed of many particles such as colloidal fluids as they become more crowded. To that end, this thesis mainly focuses on a quasi-two-dimensional (q2D) colloidal fluid that shows dynamic heterogeneous behavior and explores and develops a novel framework of data analysis to uncover above questions. As for the analysis of the dynamical feature, this thesis introduces the concept of Lagrangian coherent structures (LCSs) developed in dynamical systems theory. Basically, LCSs are moving partitions that effectively divide the fluid domain into dynamically distinct regions with qualitatively different past or future. Here we study local-heterogeneous response and transient dynamics in colloidal fluids responding against a local stimulus.

Colloidal fluids are analogous to cell motility in a sense of showing dynamic heterogeneity that is modulated by density and/or confinement. In the researches on colloidal fluids there exist several studies to quantify changes in local environments and the collectivity over many particles by referring to the measure of the local environment. In the system we investigate, the whole colloidal particles are flowing almost unidirectionally except a single particle that is optically trapped at the center and gives a precise and localized mechanical perturbation to the remaining particles at passing by the trapped particle.

Particle's responses to the perturbation are found on the space-scale of several particles diameter from the dragged particle. Indeed, these responses are spatially different at different time, and cause spatial and temporal deformation of a fluid parcel consisting of colloidal particles. How such deformations cause cage breaking and formation surrounding a reference particle is our research interest.

Quantifying the interactions in dense colloidal fluids requires a properly designed order parameter. Very frequently, the so-called bond orientational order parameter has been used to evaluate the degree of packing configuration surrounding a reference particle. However, it is known that the original definition of the bond-orientational order parameter yields discontinuous changes along time propagation of system, which hamper the appropriate elucidation of dynamical events. In this dissertation, in Chapter 2, we first present the modification of bond orientational order parameter, denoted by $\bar{\psi}_6$, that avoids discontinuous changes in time so that $\bar{\psi}_6$ provides a suitable measure to quantify the dynamics of the bond-orientational ordering of the local surroundings. Chapter 2 also provides an introductory concept of the so-called Lagrangian coherent structures (LCSs). In this dissertation, LCSs are estimated from maximum finite-time Lyapunov exponent (FTLE) field. Indeed, this maximum FTLE gives the finite-time average of the separation (stretching/divergence) between nearby trajectories. In Appendix A, we provide how one can compute the FTLE field from a set of particle trajectories.

In this system, the perturbation is attributed from the trapped probe particle to a set of the neighboring particles. This perturbation indeed propagates into the flow and causes spatial and temporal distortion of the packing structure surrounding each particle. In Chapter 3, we investigate the dynamics of the bond-orientational ordering of the local surroundings by wavelet transform. This wavelet transform provides a time-frequency representation of the time series of $\bar{\psi}_6$. From this two-dimensional scalogram plot, one can find at which time which frequency components appear in the time series. We therefore look into the frequency components of each particle that correspond to the inverse of the time scale of the perturbation in order to elucidate when nearby and/or distant particles from the trapped particle are influenced by the perturbation. It is found that particles having high power in frequencies corresponding to the frequency scale of the perturbation actually undergo distortions of their packing configuration, resulting in cage breaking and formation dynamics. Our results show that this transient cage breaking dynamics mostly appeared in the forepart of the probe particle but in a nonuniform manner. The essence of the wavelet analysis is that the conventional spatial-correlation averaged over the entire time for the order parameter is not enough to identify the spatio-temporal dynamics in this system.

Chapter 3 also provides a correspondence between the dynamic structure of cage breaking and formation of the bond-orientational ordering and the underlying dynamical structure identified by LCSs. In this thesis, we show that, the language of LCSs provides a new means for studying the heterogeneous behavior in a colloidal fluid system. When, where, and how particles undergo highly disturbance by the perturbation can be identified in terms of the spatial location of LCSs. It is shown that the spatial distribution of the FTLE field and the power of particles in the wavelet transform have a significant positive correlation, implying that LCSs provide a dynamic structure that dominates the dynamics of cage breaking and formation of the colloidal fluids.

Chapter 4 provides the conclusion and other possible application of LCSs in colloidal fluids. In this dissertation, we have analyzed LCSs in a colloidal system to probe the local-heterogeneous response to the excitation elicited by the mechanical perturbation. We discuss the applicability of the concept of LCSs to provide a deep insight into the understanding of heterogeneous dynamics of, for example, collective cell migration in response to stimuli.

Contents

List of Figures

Chapter 1

Introduction

Colloidal systems are essential to life. It may not be a common term in biology these days, but in the early 20th century, colloids were believed to hold the secrets of life. They function in every body cell, in the blood, and in all body fluids, especially the intercellular fluids. The colloidal nature of the interior of living cells motivated the study of colloidal systems. Examples of colloidal systems in molecular and cellular biology include: macromolecules such as proteins, RNA, and DNA; supramolecular assemblies such as membranes and cytoskeletal structures; bigger object such as organelles and cells.

Cell is the basic structural, functional, and biological unit for all living organisms. In biology, one of the basic components to determine the phenotype in a living body is the motion of cells. The motility of cells is a highly dynamic phenomenon that is essential to a variety of biological processes such as the embryonic development, wound healing, immune response and the cancer metastasis[1]. For example, in wound healing in animals, white blood cells and macrophages move to the wound site to kill the microorganisms that cause infection. In most of the case, cells reach their target by crawling and sometimes they are found to move collectively. This collective motion indeed refers the heterogeneity in space and time of cells motility in a living organism. Motion within a confluent epithelial cell sheet exhibits the collective migration and subcellular motion but, depending on the presence of their neighbors. At large length scales and time scales, collective migration slows as cell density rises. This behavior has an intriguing analogy to dynamic heterogeneity in a system composed of many particles as they become more crowded[2]. To that end, this thesis mainly investigates a colloidal fluid to understand the heterogeneous behavior of particles in terms of underlying dynamical feature. This colloidal fluid consists of uniform size silica beads whose dynamics are constrained in a two dimensional space, thus forming a quasi-two-dimensional colloidal system. We

expect that, this system may provide an analogy to the dynamics of confluent epithelial cell sheet.

Dynamical heterogeneity (DH) is one of the most intriguing subject in soft matter and biological physics, as it is a definite property of amorphous materials, dense colloidal fluids[3, 4], sheared granular media[5, 6] and super-cooled liquids[7, 8]. DH exists in all disordered materials with glassy transitions that occur intermittently with waiting or relaxation times that are broadly distributed. DH is usually composed of a succession of confinement events of a particle by neighboring particles. This cage effect and the breakages of the cages and transitions to diffuse, account for the variability of different relaxation timescales[9, 10]. For short times, a particle is confined by its neighboring particles in a cage whose timescale of confinement varies from place to place. On long timescales the particle manages to break its cage, so that it is able to diffuse through the entire system by successive cage breaking.

The main feature of dynamical heterogeneity involves spatial and dynamical correlations among particles that undergo large ("mobile") displacements over a suitably chosen time interval. More specifically, systems exhibit dynamical heterogeneity if (1) it is possible to select a dynamically distinguishable subset of particles and (2) these dynamics are spatially correlated. It was found that spatially correlated mobile particles move cooperatively in a fashion that they follow one another[11] and form quasi-one-dimensional, stringlike clusters[12]. Particles that are dynamically correlated can be investigated by constructing a four-point susceptibility where the dynamical correlation length grows by increasing the density of the fluid[13]. Studies of DH also include topological persistence as measured by two overlapping order parameters that quantify the correlation between particle configurations at different times[14].

Understanding DH in granular systems subject to a mechanical perturbation is of considerable interest [15–19]. Several experiments on granular systems have emphasized the role of DH under shear perturbation[5, 20] and particle dragging[21–23]. Recent experimental techniques that involve optical or magnetic tweezers coupled with optical microscopy in colloidal systems[24, 25] allow a trapped particle to provide a precise and localized mechanical perturbation to the system and to detect the response of the system simultaneously. This enables us to investigate the microscopic origin of complex fluid behavior, such as microviscosities in the shear thickening and shear thinning regimes as a function of the speed of the probe particle[26, 27]. By applying a force to the probe particle, one can explore the instantaneous and average structural responses[28] and the spatial reorganization during and after the perturbation[29]. However, the interplay between DH and the spatio-temporal behavior of the caging of particles by their neighbors is still poorly understood.

The so-called bond-orientational order parameter[30–32], ψ_6, has often been used in quasi-two-dimensional (q2D) colloidal fluids[28, 33–35], in order to quantify how nearby particles are closely packed to a reference particle, i.e., in the form of a hexagonal configuration. Dynamics of ψ_6 was studied in granular liquids near the glass transition to probe the dynamical heterogeneity and slow dynamics. There, the spatial distribution of the time-average of ψ_6 was investigated in order to extract slow dynamics of the medium-range crystalline ordered particles, whose long-range ordering is prevented by frustration effects[35]. This time-average was taken over the structural relaxation time. However, relaxation process may proceed over several timescales and some structural cage breaking and formation may occur in shorter times than a timescale used for the time-averaging. If so, it is difficult to determine properly when and how the structural breakage and formation events happen and which particles are involved in those structural events in terms of the time-averaged spatial distribution of the bond-orientational order parameter.

In this thesis, we focus on the time dependence and spatial extent of bond-orientational ordering around individual particles in order to see how colloidal particles are involved in the cage breaking and formation dynamics in response to a microscopic perturbation. Indeed, this perturbation is attributed directly from the particle which is trapped at the center and indirectly from the fluid moving around the trapped particle [28]. We first introduce a modified bond-orientational order parameter, denoted by $\bar{\psi}_6$, to properly quantify the time evolution of bond-orientational ordering. This overcomes some drawbacks that exist in the original definition of ψ_6. From the time evolution of $\bar{\psi}_6$ we observe that the size of temporal fluctuation in the magnitude of $\bar{\psi}_6$, not the magnitude of $\bar{\psi}_6$ itself, reflect the extent of distortion in the surrounding particles, i.e., cage breaking and formation. To see when and which particles participate in the cage breaking and formation dynamics, we perform a time-frequency analysis by continuous wavelet transforms for the time series of $\bar{\psi}_6$. Basically, wavelet transform enable us to provide a time-frequency representation of a time series of interest. From this two-dimensional scalogram plot, one can find at which time and which frequency components occur in a time series. It is found that particles having frequency components similar to that of the inverse of the timescale of perturbation are involved in cage breaking and formation.

To look further into the origin of cage breaking and formation, we introduce the concept of Lagrangian Coherent Structures (LCSs) developed in dynamical systems theory[36–38], which effectively divide the flow into distinct regions with qualitatively different past or future. A number of applications have been studied through LCSs including cell behavior[39], blood flow mechanics inside blood vessels[38] and hearts[40], prey-predator interaction in jelly fish feeding [41], particle dynamics [42], etc. However most of the previous studies related to biological systems were discussed by a model simulation.

Here, we study local heterogeneous responses and transient dynamics in colloidal fluids responding against a stimulus.

In this thesis, LCSs refer to the location of large magnitude in the finite-time Lyapunov exponent (FTLE) field where FTLE measures the maximum separation rate between nearby trajectories over a finite time interval. Due to the characteristic of FTLE ridges, their spatio-temporal location is expected to affect the nearby packing configuration of the colloidal particles within the corresponding separation timescale. It is found that the spatio-temporal distribution of the FTLE field and the power of the particles in the wavelet transform, both computed for the same timescale, have a positive correlation, showing that FTLE based LCSs, denoted by FTLE/LCSs[42], provides a dynamic structure that dominates the dynamics of cage breaking and formation of the colloidal fluids.

This thesis is organized as follows: In chapter 2 we briefly describe the experimental system we study, overview and discuss some drawbacks of the original bond-orientational order parameter, provide a modified bond-orientational order parameter, and introduce the concept of FTLE/LCSs. Chapter 3 contains the investigation of the time series of the $\bar{\psi}_6$, the wavelet analysis to investigate the cage breaking dynamics, the results of FTLE/LCSs that probe the dynamical heterogeneity and the relationship between FTLE/LCSs and cage breaking dynamics. We provide conclusions and outlook in chapter 4.

Chapter 2

System and Method

2.1 A quasi-two-dimensional (q2D) system with a mechanical perturbation

The quasi-two-dimensional (q2D) experimental system considered in this thesis was described in detail in Ref. [28]. The sample consists of an aqueous suspension of uniform size silica spheres (diameter $d = 2.56 \pm 0.04\mu$m) and the suspension is confined between two hard walls with height (separation) of 3.2 μm, i.e., slightly larger than the particle diameter. A particle is optically trapped at the center by a 810 nm laser beam with a force constant $k = 0.2$pN/nm. The stage containing the suspension is moved at a constant speed v and thus the trapped particle interacts with and causes a mechanical perturbation to the system. The case considered has an average packing fraction of ~ 0.76. Note that the experimental data are collected in the reference frame of the trapped particle and the stage moves with a constant speed. One can easily transform the data into the dragged reference frame where the probe particle is dragged at constant speed and the stage is stationary. We do our analysis in the trapped reference frame. Note however that the quantities we analyze are frame-independent, i.e., do not depend on the reference frame in which one observes the system dynamics.

2.2 Bond-orientational order parameter and its drawback

How can one quantify spatio-temporal heterogeneity of local environments in the neighborhood of individual particles in colloidal fluids under a mechanical perturbation? In a quasi-two-dimensional (q2D) colloidal fluid, the packing structure around a particle of interest can be quantified by the so-called bond-orientational order parameter ψ_6^j defined

as[33–35, 43],

$$\psi_6^j = \frac{1}{n_j}\Big|\sum_{k=1}^{n_j}\exp(i\cdot 6\theta_k^j)\Big| \tag{2.1}$$

for each particle j, where the sum runs over n_j nearest neighbors around particle j, and θ_k^j is the angle between an arbitrary fixed axis and the link of particle j and its k-th nearest neighbor as shown in Fig. 2.1. In Eq. 2.1, the summand term refers to the configuration of the first neighboring cage, and n_j is the corresponding number of the first neighboring particles around particle j. Usually, n_j is chosen either as a constant of value six, i.e., six nearest neighbors,[28, 34] or as a variable dependent on local coordination around particle j (first nearest neighbors) defined by using a Voronoi construction[33, 35, 43]. The denominator n_j is used to normalize ψ_6^j as $0 \le \psi_6^j \le 1$. The value $\psi_6^j = 1$ implies perfect hexatic order solely with six nearest neighboring particles, whereas $\psi_6^j \ll 1$ implies a region deviating from hexatic order.

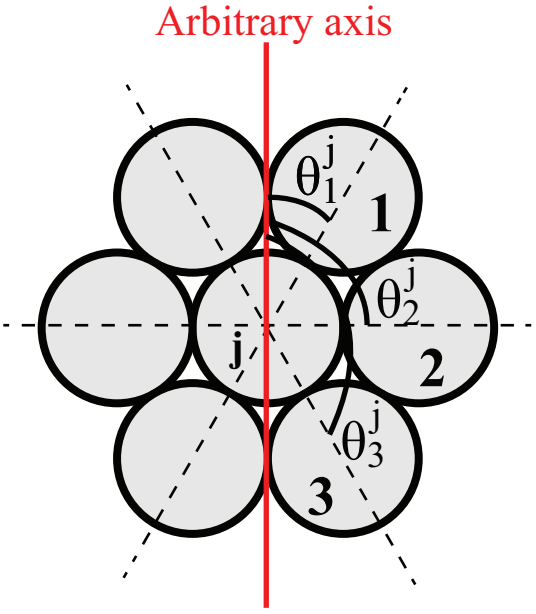

FIGURE 2.1: Schematic picture of θ_k^j, angle between an arbitrary axis (red line) and the link (dotted lines) of the particle j and its k-th (e.g. $k = 1, 2, 3$) nearest neighbor.

Previously, on this system[28], the orientation of the structural order around a particle j was investigated by another index defined by

$$\widetilde{\psi}_6^j = \mathrm{Re}\{\sum_{k=1}^{6}\exp(i\cdot 6\theta_k^j)\} \tag{2.2}$$

where θ_k^j is the angle between a fixed axis and the line connecting the centers of particle j and its k-th nearest neighbor. The fixed axis was assumed along the dragging direction of the probe particle in the dragged reference frame. To this end, $\widetilde{\psi}_6^j$ was varied as

$-6 \leq \widetilde{\psi}_6^j \leq 6$ where the sign reports the orientation of the hexatic structure relative to the dragging direction. That is, 6 and -6 indicates the orientation of the hexatic structure along the direction of dragging and of an angle 30° from the dragging direction, respectively. Within a regular hexagonal domain $\widetilde{\psi}_6^j$ become constant. Changes in the value of $\widetilde{\psi}_6^j$ refer the grain boundaries and transitions to disordered domains. It was found that, in the dragged reference frame, the displacement of some individual particles thus forming a displacement chain, responding to a displacement of the probe particle, propagates according to the orientation of the local hexatic structure. In other words, the displacement chains form inline when $\widetilde{\psi}_6^j > 0$ and bifurcate when $\widetilde{\psi}_6^j < 0$. Some displacement chains were found to follow the grain boundaries indicating that the local order and defects influence the particles' response to the disturbance attributed from the probe particle. However, the value of $\widetilde{\psi}_6^j$ does not necessarily provide the proper knowledge of the packing configuration surrounding a particle j. For example, $\widetilde{\psi}_6^j = 0$ can result from the two possible situations. One is the packing configuration surrounding a particle j is far from a hexatic order. The other extreme case is that there is a perfect hexatic order but its orientation with respect to the fixed axis (along dragging direction in Ref. [28]) is 15°. Therefore, in order to quantify the proper structural configuration surrounding an individual particle, in our analysis we use ψ_6^j as defined in Eq. 2.1. Note that, differences in the values of ψ_6, obtained from Eq. 2.1, also have been used to assign frozen (ordered) and mobile (disordered) regions, termed grain and grain boundary (GB) regions, with some high and low values of ψ_6, respectively[34].

Particles in the GB regions are loosely packed and are identified as mobile particles compared to those in the grain regions. It was pointed out that some of these mobile particles move "cooperatively" associated with breakage of their neighboring cages[34]. This cooperative motion was determined by the criterion, so-called Donati string criterion[11]. The criterion states that one particle is moved and another particle takes it place after time Δt as illustrated in Fig. 2.2. In the figure, the light circles correspond to the position of particles at time $t = t_0$ and the dark ones correspond to the same particle at later time $t^* = t_0 + \Delta t$. Viewing the particles' position at two different times as in Fig. 2.2, it was observed that these particles are moving cooperatively along string like paths[11, 12]. Using the Donati criterion, it was found that the string particles are localized in GB regions[34]. They can be visualized by a snapshot of bond-orientational structure overlaying the string particles at the high packing fraction of 0.85 [34]. However, at (comparatively) lower packing fraction, e.g., ~ 0.76 in our q2D colloidal fluid system experiencing the constant dragging perturbation[28], ordered and disordered regions are sparsely distributed and they are not directly related to the mobility of the particles. For example, particles in remote regions having lower values of ψ_6 simply

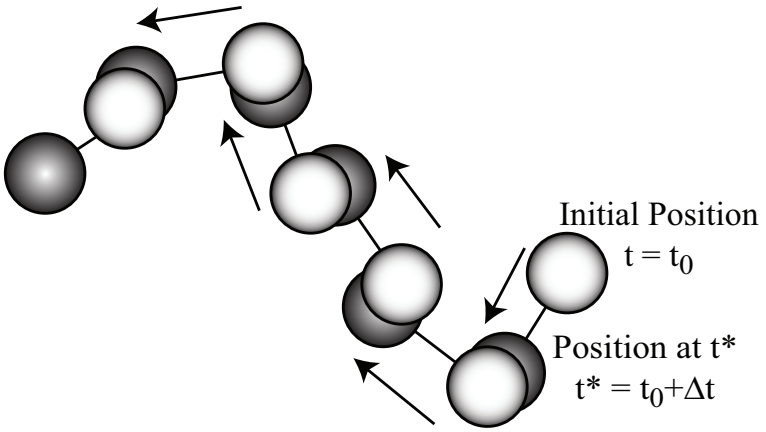

FIGURE 2.2: Schematic picture of the Donati criterion. Light circle: particles at the initial position $t = t_0$. Dark circle: same particles at a later time $t^* = t_0 + \Delta t$. The black line segments connect the same particles at the two times. The arrows indicate the path followed by some of the particles.

passing along the flow applied to the colloidal system while maintaining the low ψ_6 values. Furthermore, for constant dragging perturbation, the forced motion of the probe particle distorts its bond-orientational structure by repeatedly breaking its neighboring cages and leads to the extension of GB and disordered region[28].

To demonstrate it, Fig. 2.3 shows two representative snapshots of the distribution of ψ_6 of colloidal particles. In Fig. 2.3(a) some particles in front of the center particle along the steady flow (indicated by the green ellipse) get stuck and are slowed down for some time duration and have a large ψ_6 values (i.e., ordered). However, in Fig. 2.3(b) at some later time, the ordered region disappears and becomes disordered with smaller ψ_6. In fact, regions of large and small ψ_6 vary in time and sometimes exchange with each other. Thus the instantaneous distribution of ψ_6 does not necessarily capture the imminent heterogeneous nature of the frozen and mobile regions. In this regard, the time variation of ψ_6 is more insightful to understand how the perturbation induces the rearrangement of particles' positions.

In quantifying the time evolution of packing structure around individual particles in colloidal fluids, some disadvantages emerge for the bond-orientational order parameter especially at packing fractions, e.g., 0.72-0.79. In Eq. 2.1, the summand term takes into account only the orientation (or angular position) of the neighboring particles. Therefore ψ_6 gives the same value for the different cases shown in Figs. 2.5(a) and 2.5(b) since the angular positions of the surrounding particles are the same.

Another problem is in the identification of the number of neighboring particles around particle j, n_j. One common choice is $n_j = 6$, that is, six nearest neighbors surrounding any particle of interest[28, 34]. However, when a particle is surrounded by more than

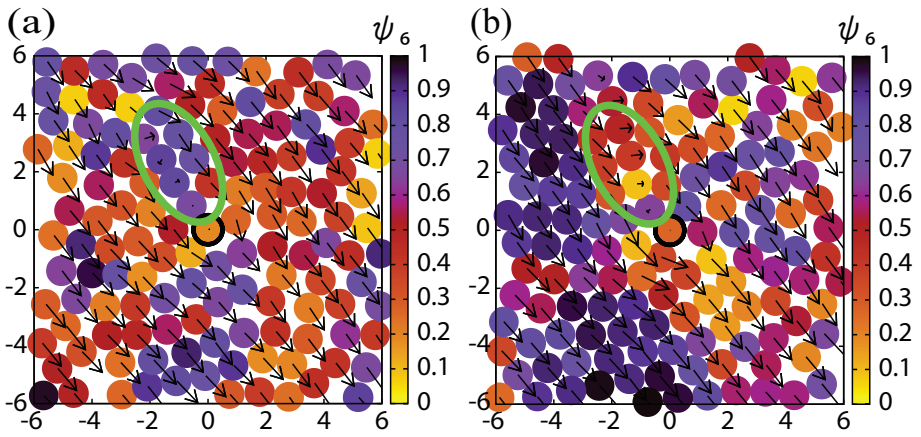

FIGURE 2.3: (a) and (b) are two snapshots of ψ_6 of colloidal particles with their displacement vector under the steady flow from the left top to the right bottom, where the center particle trapped by the optical tweezer as outlined by black bold circle. The particles enclosed by the green line show a typical behavior of particles in front of the center particle. See Sec. 2.2

six particles in the first neighboring shell as described schematically in Fig. 2.5(c,d,e) (it was found that about 12% of all particles have more than six particles there in our system), the identification of six *nearest* neighbors may change from time to time due to the fluctuation in positions. Therefore, ψ_6 may change discontinuously in time for particles that have more than six neighboring particles in the first shell for a certain time duration even when the actual configurational change of neighboring particles is smooth.

Another choice for n_j is to determine the neighboring particles by using Voronoi tessellation [35, 43]. Voronoi tessellation or Voronoi diagram is a way of partitioning space with a set of points, called sites, into convex polygons such that each polygon contains exactly one site. Every point in each convex polygon is closer to that site than to any other. The polygons are called Voronoi cells. As for simple illustration, Fig. 2.4 shows Voronoi tessellation for a set of 16 sites $\{P_1, P_2, \cdots, P_{16}\}$ in the Euclidean plane $\mathbb{R}^2$. In this case each site $P_k \in \{P_1, P_2, \cdots, P_{16}\}$ is simply a point. The Voronoi cell R_k associated with the site P_k contains all the points whose distance to P_k is not greater than their distance to the other sites than P_k. In other words, if $D(y, P_k)$ is defined as an Euclidean distance, then the Voronoi cell R_k is defined as $R_k = \{y \in \mathbb{R}^2 | D(y, P_k) \leq D(y, P_j) \forall j \neq k\}$. The equality refers the segments in a Voronoi tessellation corresponding to all points in the plane equidistant to the two nearest sites. Fig. 2.5(f,g,h) show the samples of Voronoi tessellation for the colloidal particles whose centers are regarded as sites. Here we construct the Voronoi tessellation using the software *Mathematica*.

For each Voronoi cell, Voronoi vertices are the points equidistant to three (or more) sites.

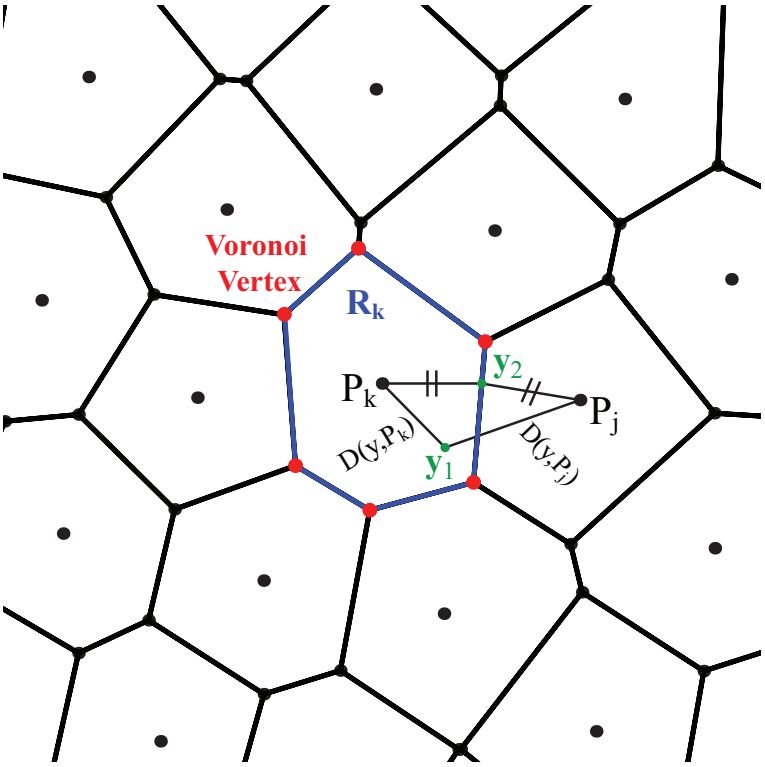

FIGURE 2.4: Voronoi tessellation for a set of 16 sites in the Euclidean plane. A Voronoi cell R_k associated with the site P_k is shown by a blue polygon whose Voronoi vertices are indicated by red circle. The cell contains all the points $y \in \mathbb{R}^2$ whose distance to P_k is less than that from the other site P_j, i.e. $D(y_1, P_k) \leq D(y_1, P_j)$. Points on the edges of the Voronoi cell are equidistant to the two nearest sites, i.e. $D(y_2, P_k) = D(y_2, P_j)$.

To that end, Voronoi vertices are connected with three (or more) edges making a triangular (or more) network and particles sharing those edges are counted as neighboring particles. As indicated by the red circle in Fig. 2.5(f,g,h), a new short length's edge that may emerge in time as shown in Fig. 2.5(h) also results in a discontinuous change in the number of the neighboring particles. That is, if one of the edges becomes very short compared to the others, the corresponding triangular network becomes unstable due to the fluctuation of the particles' position. After a certain moment, another triangular network may develop at that location. As a result, the number of neighboring particles can change discontinuously and this causes (unphysical) discontinuous jumps in the values of ψ_6. This is not favorable in the study of the dynamics of packing structure, i.e., cage breaking and formation dynamics. At high packing fraction, the above problem may not be so significant because particles are densely packed and they have very little space to fluctuate. However at a relatively low packing fraction, such as ~ 0.76 in our study, one will be immediately confronted to the above drawbacks in computing the bond-orientational order parameter. Therefore, some modification is needed to eliminate these drawbacks.

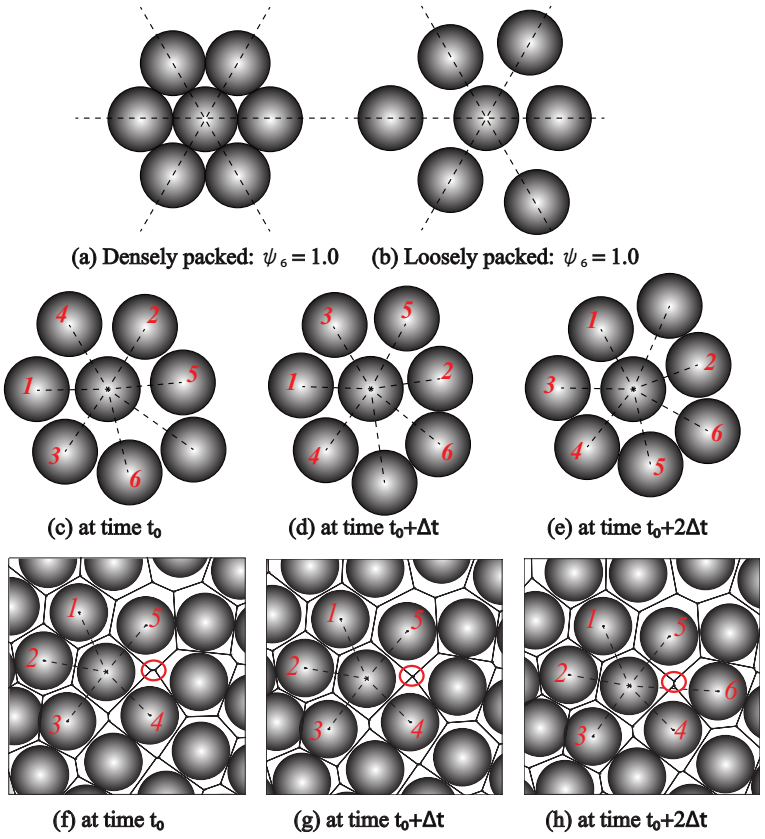

FIGURE 2.5: (a) Densely packing and (b) loosely packing structures. Both return the same value of $\psi_6(=1)$. (c, d, e) One particle is surrounded by seven particles but which particles are the six nearest neighbors are different from time to time because of the fluctuation of their distance from the center particle. (f, g, h) Voronoi construction at successive time instants. Fluctuations in the particle positions result in different constructions in (g) to (h) because one triangular network in (f) becomes unstable in (g) and developed another network at that location in (h) as indicated by the red circle.

2.3 A modified bond-orientational order parameter $\bar{\psi}_6$

We present a modified bond-orientational order parameter $\bar{\psi}_6$ to properly quantify the dynamical evolution of local packing structure. This parameter is defined as

$$\bar{\psi}_6^j \equiv \frac{|\sum_k' w(|\mathbf{r}_k - \mathbf{r}_j|) \exp(i \cdot 6\theta_k^j)|}{c_0}, \tag{2.3}$$

where the summation $\sum_k'$ runs over all particles except the jth particle, θ_k^j is the angle between an arbitrary fixed axis and the link of the particles k and j whose positions are denoted by $\mathbf{r}_k$ and $\mathbf{r}_j$, respectively, c_0 is the maximum possible value of the denominator in case that the whole system attains perfect order (i.e., making $\bar{\psi}_6^j$ normalized as $0 \leq \bar{\psi}_6^j \leq 1$). The weight function $w(r) = \exp(-\frac{(r-d)^2}{2\sigma^2})$, d is the diameter of each particle. This weight function $w(r)$ takes into account the distance between the surrounding

particles and the particle of interest. In order to choose the value of σ, we estimate the size of the first neighboring shell in terms of the radial distribution function. The radial distribution function $g(r)$ is a measure of the probability of finding a particle at a distance r from another particle[44]. The general algorithm involves, first, calculating the distance between all particle pairs, second, these distances are sorted into a histogram where each bin has a width dr. The histogram is then normalized with respect to an ideal gas, where particle histograms are completely uncorrelated. For two dimensional system, this normalization is the number density $\rho = N/A$, N is the total number of particles and A is the area, of the system multipled by the area of the shell that extends from r to $r + \mathrm{d}r$. This normalization constant can be expressed by $N_{id} = \rho\pi[(r + \mathrm{d}r)^2 - r^2]$. Mathematically, for two dimensional system, $g(r)$ is formulated by

$$g(r) = \frac{1}{NT'N_{id}} \sum_{t=1}^{T'} \sum_{i=1}^{N} \sum_{\substack{j=1 \\ j\neq i}}^{N} \delta\big[r - r_{ij}\big] \tag{2.4}$$

where $r_{ij} = \big\|\mathbf{r}_i(t) - \mathbf{r}_j(t)\big\|$, $\mathbf{r}_i(t)$ is the position of particle i at time t, δ is the Dirac's delta function, and T' is the total number of frames. Fig. 2.6 shows the radial distribution function for our colloidal system with the bin size $0.1d$. The first minimum in $g(r)$ provides the characteristic length scale of the first neighboring shell. Outside of the first neighboring shell, i.e. $1.5 \leq r/d$, a number of obvious peaks indicate that the particles are ordered and packed around each other in the neighboring shells. At long range, $g(r)$ tends to a value of 1, indicating that particles in that range are uniformly distributed.

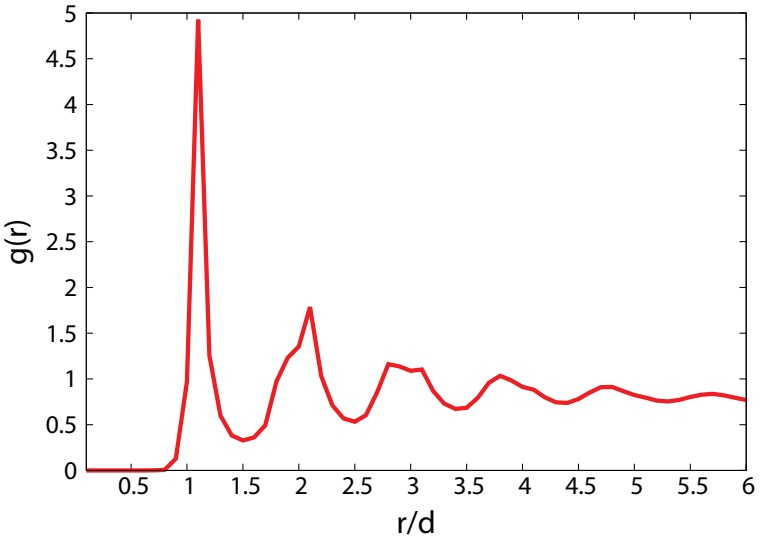

FIGURE 2.6: Average radial distribution function of a colloidal fluid with an average packing fraction of 0.76. The Péclet number (Pe) for the dragging is 190. This radial distribution function is calculated by using configurations of the colloidal fluid observed for 74.61s with frame rate 67 Hz.

In our system the radial distribution function has the well-defined first minimum placed at approximately $1.5d$ as seen in Fig. 2.6. In our system σ is chosen so that particles in the first neighboring shell lie within two standard deviations, $2\sigma = 1.5d - d = 0.5d$ from the mean d, and hexagonal configurations such as Fig. 1(a,b) can be distinguished (e.g., $\bar{\psi}_6$, returns 1.0 and 0.567 for the configurations in Fig. 2.5(a) and Fig. 2.5(b), respectively). Another advantage is that this formula does not require identifying the neighboring particles, and is therefore free from any discontinuous identification of neighboring particles. Note that $\bar{\psi}_6$, like the original ψ_6, is a frame-independent measure.

2.4 Lagrangian Coherent Structures (LCSs)

In this section, we introduce another concept, Lagrangian Coherent Structures (LCSs), to investigate underlying mechanism behind cage breaking and formation. The concept of Lagrangian Coherent Structures was first introduced by Haller[36, 37] and has received significant attention for understanding transport phenomena in finite-time non-autonomous dynamical systems. Briefly, LCSs serve as robust transport barriers between regions in which particles have different dynamical behavior. By definition, LCSs are an invariant manifold across which any particle cannot traverse. Thus they are barriers to transport between the regions of different dynamics. Such structures can be characterized as co-dimension one (lines in two-, surfaces in three-dimensions) and play the dominant role in attracting, repelling or shearing of neighboring trajectories over a finite time interval $[t_0, t_1]$. Fig. 2.7 shows a schematic description of repelling and sheared type LCSs. Fig. 2.7(a) depicts a fluid parcel containing a set of particles initially at time $t = t_0$ is deformed along the normal direction to the repelling LCSs as it repels strongly the nearby fluid particles by time $t = t_1$. Fig. 2.7(b) depicts a fluid parcel that deforms along the tangential direction to the sheared LCS as the particles in the upper side move faster than those of the lower side.

The cornerstone of this structure is the frame-invariance property. To that end, when defining LCSs, the fluid motion is viewed from a Lagrangian, rather than an Euler perspective. A number of phenomena have been studied through LCSs including cell behavior[39], blood flow mechanics inside blood vessels[38] and hearts[40], prey-predator interaction in jelly fish feeding [41], particle dynamics [42], etc.

Based on the numerous application of LCSs, the most efficient and simplest diagnostic tool for identifying LCSs would be to identify the ridges or the location of high magnitude in the finite-time Lyapunov exponent (FTLE) field[45]. Basically, at each location of the ridges, the FTLE possesses the maximum separation rate between nearby trajectories over a finite time interval. Maximum ridges of the FTLE field in forward-time

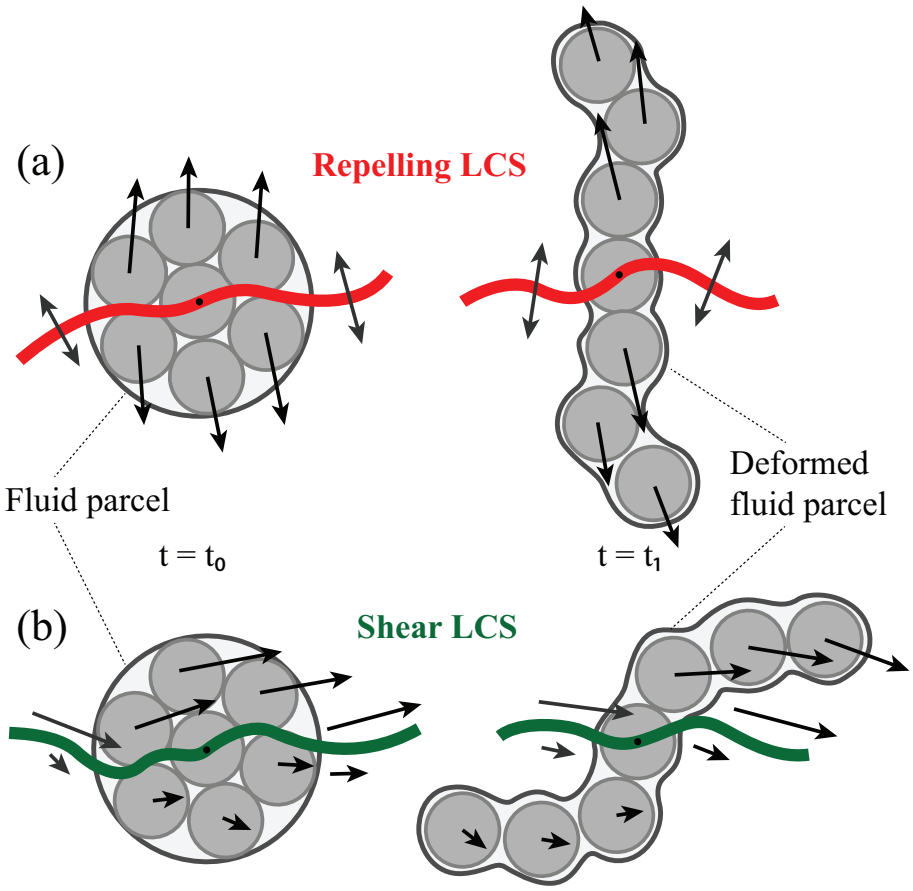

FIGURE 2.7: Two types of deformation of a fluid parcel containing a set of particles over the time interval $[t_0, t_1]$. (a) For repelling LCS, this deformation occurs normal to it and (b) for shear type LCS, such deformation occurs tangential to it.

propagation are indicators of repelling LCSs that are the regions of the locally strongest diverging flow in the system[46, 47]. Performing the same procedure in backward-time propagation can identify maximum ridges of the backward-time FTLE field. The regions of the locally strongest diverging flow backward in time are, in fact, those of the locally strongest converging flow in ordinary forward-time propagation, corresponding to attracting LCSs in the system.

2.4.1 Mathematical background of LCSs

First let $\mathbf{x}(t; t_0, \mathbf{x_0}) \in \mathbb{R}^2$ be the position of a particle at time $t \in \mathbb{R}$, which starts from the initial position $\mathbf{x_0} = \mathbf{x}(t_0; t_0, \mathbf{x_0})$ at time $t = t_0$. Here we consider two dimensional space because the system in this study can be regarded as a two-dimensional system as the motion of particles are confined between two hard walls and the height (distance) between two walls is only 1.5 times the diameter of particles[28]. By following particle trajectories over a duration of time T after initial time t_0, we obtain a particle flow map

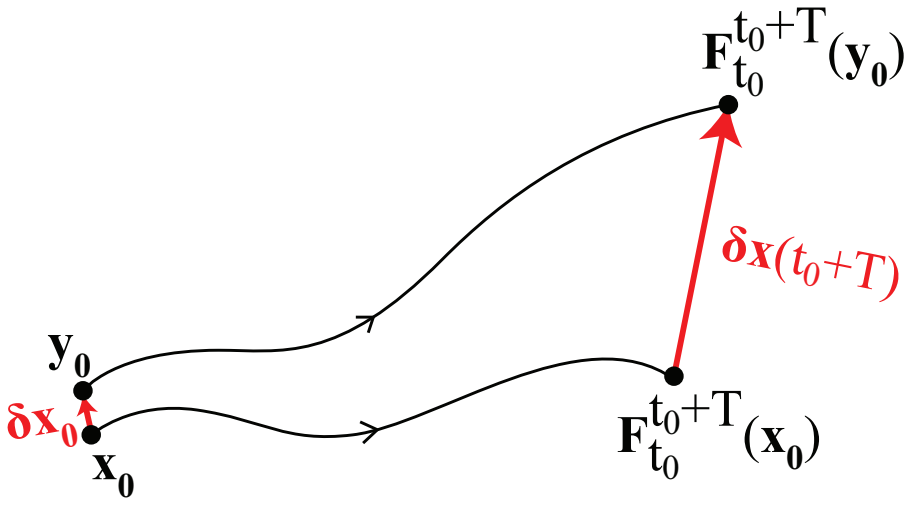

FIGURE 2.8: Figure shows the propagation of small initial displacement $\delta\mathbf{x_0}$ to $\mathbf{x_0}$ at the initial time t_0. The flow map $\mathbf{F}_{t_0}^{t_0+T}(\mathbf{x_0})$ takes particles from their initial position $\mathbf{x_0}$ to their position at time $t_0 + T$.

$\mathbf{F}_{t_0}^{t_0+T}(\mathbf{x_0}) = \mathbf{x}(t_0 + T; t_0, \mathbf{x_0})$ that takes particles from their initial position $\mathbf{x_0}$ to their position at time $t_0 + T$.

To locate LCSs, we compute the FTLE field of the flow map. We consider a trajectory $\mathbf{x_0}$ and a nearby displaced trajectory $\mathbf{y_0} = \mathbf{x_0} + \delta\mathbf{x_0}$, where $\delta\mathbf{x_0}$ is an arbitrary small initial displacement at time t_0 to $\mathbf{x_0}$ as shown in Fig. 2.8. By the advection of the flow, the propagation of this displacement by time $t_0 + T$ is given by,

$$\delta\mathbf{x}(t_0 + T) = \mathbf{F}_{t_0}^{t_0+T}(\mathbf{y_0}) - \mathbf{F}_{t_0}^{t_0+T}(\mathbf{x_0}) = \frac{\mathrm{d}\mathbf{F}_{t_0}^{t_0+T}(\mathbf{x_0})}{\mathrm{d}\mathbf{x_0}}\delta\mathbf{x_0} + \mathcal{O}\Big(\|\delta\mathbf{x_0}\|^2\Big) \tag{2.5}$$

where $\frac{\mathrm{d}\mathbf{F}_{t_0}^{t_0+T}(\mathbf{x_0})}{\mathrm{d}\mathbf{x_0}}$ is the Jacobian of the flow map. By dropping higher-order terms of $\delta\mathbf{x_0}$, the magnitude of $\delta\mathbf{x}(t_0 + T)$ is given by,

$$\begin{aligned}\big\|\delta\mathbf{x}(t_0 + T)\big\| = \left\|\frac{\mathrm{d}\mathbf{F}_{t_0}^{t_0+T}(\mathbf{x_0})}{\mathrm{d}\mathbf{x_0}}\delta\mathbf{x_0}\right\| &= \sqrt{\left\langle \frac{\mathrm{d}\mathbf{F}_{t_0}^{t_0+T}(\mathbf{x_0})}{\mathrm{d}\mathbf{x_0}}\delta\mathbf{x_0}, \frac{\mathrm{d}\mathbf{F}_{t_0}^{t_0+T}(\mathbf{x_0})}{\mathrm{d}\mathbf{x_0}}\delta\mathbf{x_0}\right\rangle} \\ &= \sqrt{\left\langle \delta\mathbf{x_0}, \mathbf{C}_{t_0}^{t_0+T}(\mathbf{x_0})\delta\mathbf{x_0}\right\rangle}\end{aligned} \tag{2.6}$$

where $< \cdot, \cdot >$ is the standard inner product on $\mathbb{R}^2$, $\mathbf{C}_{t_0}^{t_0+T}(\mathbf{x_0}) = \left(\frac{\mathrm{d}\mathbf{F}_{t_0}^{t_0+T}(\mathbf{x_0})}{\mathrm{d}\mathbf{x_0}}\right)^* \frac{\mathrm{d}\mathbf{F}_{t_0}^{t_0+T}(\mathbf{x_0})}{\mathrm{d}\mathbf{x_0}}$ is the finite-time right Cauchy-Green deformation tensor, a rotation and translation invariant measure of deformation. The symbol * refers to matrix transposition. Since $\mathbf{C}_{t_0}^{t_0+T}(\mathbf{x_0})$ is a symmetric and positive definite tensor, all the eigenvalues of this tensor are real and positive. The eigenvectors associated with the eigenvalues are orthonormal to each other. The growth of the initial displacement $\delta\mathbf{x_0}$ will become maximum when

it is aligned with the eigenvector corresponding to the largest eigenvalue of $\mathbf{C}_{t_0}^{t_0+T}(\mathbf{x_0})$. That is, if $\lambda_{\max}\big(\mathbf{C}_{t_0}^{t_0+T}(\mathbf{x_0})\big)$ is the maximum eigenvalue of $\mathbf{C}_{t_0}^{t_0+T}(\mathbf{x_0})$, then

$$\big\|\delta\mathbf{x}(t_0+T)\big\| = \sqrt{\lambda_{\max}\big(\mathbf{C}_{t_0}^{t_0+T}(\mathbf{x_0})\big)}\big\|\delta\mathbf{x_0}\big\|. \tag{2.7}$$

The largest finite-time Lyapunov exponent (FTLE) represents the maximum linear growth rate of a small initial displacement over a finite time interval $[t_0, t_0+T]$ and is defined as[36]

$$\Lambda_{t_0}^{t_0+T}(\mathbf{x_0}) = \frac{1}{|T|}\ln\left\|\frac{\delta\mathbf{x}(t_0+T)}{\delta\mathbf{x_0}}\right\| = \frac{1}{|T|}\ln\sqrt{\lambda_{\max}\big(\mathbf{C}_{t_0}^{t_0+T}(\mathbf{x_0})\big)}. \tag{2.8}$$

According to this definition, The FTLE can be considered as a measure of how the trajectories are sensitive to the initial condition. Also, due to the frame-independence of the Cauchy-Green deformation tensor, the FTLE field is independent of the choice of the reference frame. Basically, the largest eigenvalue and the corresponding eigenvector provides the maximal amount and the maximal principal stretching direction of the deformation of a fluid parcel. The distribution of the FTLE field in the phase space can be used to locate the maximum deformation of a fluid parcel in the dynamical system. Here, the locations of the high magnitude of FTLE values in the FTLE field are used to identify Lagrangian Coherent Structures(LCSs)[48] and denoted by FTLE/LCSs.

2.4.2 Computation of FTLE/LCSs

There are four steps involved in computing the FTLE field defined by Eq. 2.8. Firstly, a set of virtual particles are placed on an initial grid with a uniform spacing of $0.0125d$ at the initial time t_0 in the domain of interest. Next, by the advection of the flow, the particles are allowed to move from the initial time t_0 to the final time t_0+T. The trajectories of the particles at time t can be obtained by constructing the flow map from instantaneous tracking[42, 49] of colloid particle positions from the experimental data. The details of the construction of the flow map is discussed in the Appendix A. Once the flow map is obtained, next step is to compute the Jacobian of the flow map, usually by finite differencing, to obtain the Cauchy-Green deformation tensor. Finally, the largest eigenvalue of the tensor is extracted and synthesized into a FTLE field as in Eq. 2.8. Indeed, the FTLE value is computed for each particle in the grid and assigned to the particle location at time t_0. This process is repeated for various initial times t_0 to get the time evolution of the FTLE field. In general, one can choose an integration time corresponding to the timescale of the dynamics of interest. However, it is not desirable to choose the integration time larger than the timescale in which all the particles are advected out from the spatial domain.

Chapter 3

Results and discussion

In this chapter, we investigate the dynamics of the bond-orientational ordering of the local surroundings by wavelet transform. This wavelet transform provides a time-frequency representation of the time series of $\bar{\psi}_6$. From this two-dimensional scalogram plot, one can find at which time which frequency components appear in the time series. We therefore look into the frequency components of each particle that correspond to the inverse of the time scale of the perturbation in order to elucidate when nearby and/or distant particles from the trapped particle are influenced by the perturbation. This chapter also provides a correspondence between the dynamic structure of cage breaking and formation of the bond-orientational ordering and the underlying dynamical structure identified by LCSs. We show that, the language of LCSs provides a new means for studying the heterogeneous behavior in a colloidal fluid system.

3.1 Investigation of the time series of $\bar{\psi}_6$

Fig. 3.1 shows a representative snapshot of $\bar{\psi}_6$ at one time instant, which shows that, at this packing fraction of ~ 0.76, there exist no clear grain and grain boundary regions. Turning to the time evolution of $\bar{\psi}_6(t)$, it has been found that $\bar{\psi}_6(t)$ of the center particle, which is optically trapped, exhibits the largest fluctuation along the time propagation. Some other particles also exhibit a similar large variation of $\bar{\psi}_6(t)$ when they are passing through the neighborhood of the center particle and/or in front of the center particle. Fig. 3.2 exemplifies the time evolution of $\bar{\psi}_6(t)$ for some randomly selected particles. In the plot at the lower-middle image of the figure, each colored circle represents the position of a randomly selected colloidal particle at a certain time instant with a line passing through the circle corresponding to the trajectory of the corresponding particle. The number inside the circle is the particle's index. The trapped particle is located at

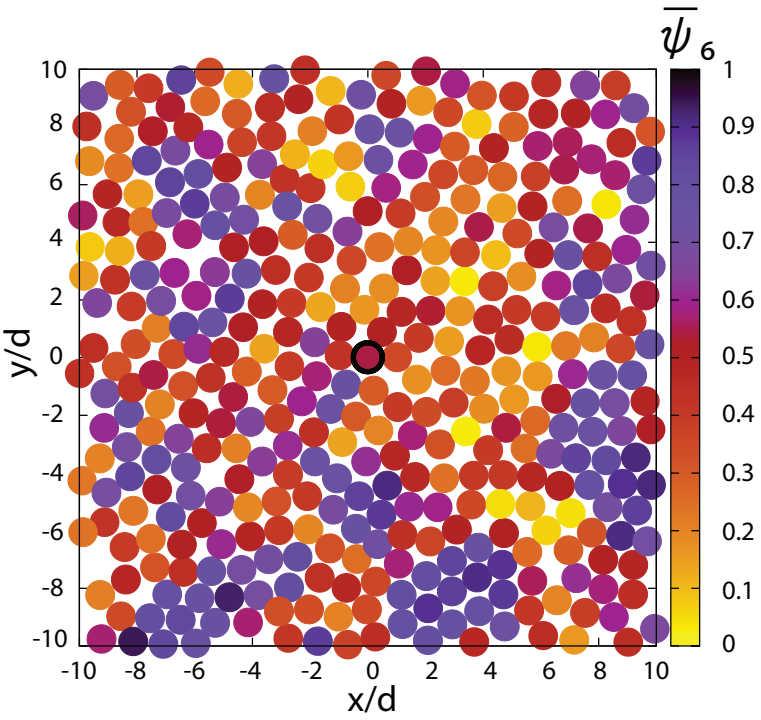

FIGURE 3.1: A snapshot of $\bar{\psi}_6$ in the colloidal fluids at the packing fraction of ~ 0.76. The darker (the lighter or the more yellowish) the color, the closer (the looser) to hexagonal packing the nearby configuration is.

the center. The time series of $\bar{\psi}_6(t)$ of the selected particles are superposed to that of $\bar{\psi}_6(t)$ of the probe particle, as indicated by the red line. From the superposition of the time series, we can see that variations of $\bar{\psi}_6(t)$ for particles 119, 137, 221, 235, at some time duration, are roughly similar to those of the probe particle as indicated by dotted ellipses. In fact, at these time durations the corresponding particles are passing through the neighborhood of the probe particle. However, for particle 354, such a significant local and fast fluctuation of $\bar{\psi}_6(t)$ seems not to exist; it simply "passively" passes through the remote region from the center particle.

Fig. 3.3 illustrates the underlying configurational changes corresponding to the fluctuation of $\bar{\psi}_6$ for the center particle (indicated by the red circle) and two other particles of index 119 and 137 (blue circles). Here the particles surrounding the center particle, and also particles of index 119 and 137, are chosen within the radial distance of $1.5d$ from them (since particles in the first neighboring shell lie within $1.5d$ from a particular particle). The vectors (magnified by two times) on the particle represent their displacements in time $0.5d/v$. Fig. 3.3(a) shows that the packing structure for the probe particle is repeatedly breaking and more likely forming in a hexagonal shape which is quantified by $\bar{\psi}_6$. One can see that for the center particle, this fluctuation more likely occurs in the timescale ($\sim d/v$) as the center particle needs to move one particle's diameter

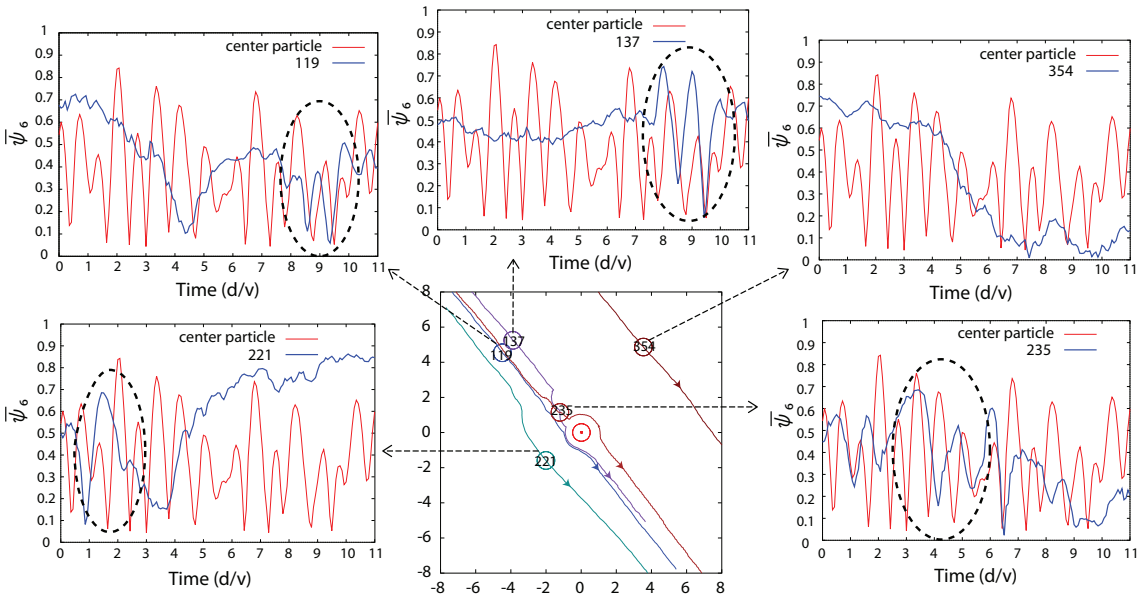

FIGURE 3.2: Time series of $\bar{\psi}_6(t)$ of some randomly chosen particles, as shown in the lower-middle panel, is superposed to that of the probe particle for comparison. The unit of time on the horizontal axis is d/v where d and v denotes, respectively, the diameter of each particle and the constant speed applied to the system except the trapped probe particle. One can see that the time period of one oscillation in the fluctuation of $\bar{\psi}_6(t)$ of the probe particle is found to be an order of unity in the unit of d/v.

(d) through breaking its first neighboring cage at the constant speed v. Within this timescale, the surrounding medium will also be perturbed and this perturbation causes a rearrangement of the packing structure around some other particles. For example, in Fig. 3.3, particles of index 119 and 137 show that, along the plateau regions of $\bar{\psi}_6(t)$, that is, from 6 to 7.5 d/v for particles 119 and 137, their packing configuration is not changing significantly. In this time regime, surrounding particles simply move parallel to the constant velocity vector $\boldsymbol{v}$ applied to the system and the displacement vectors of the surrounding particles are similar to each other. However, whenever the displacement vectors of the surrounding particles become not in parallel, $\bar{\psi}_6(t)$ starts to fluctuate with large amplitude. Such large fluctuation starts from $\sim 8d/v$ for both the particles when some nearby particles seem to get stuck and slow down as illustrated by the displacement vectors. This shows that fluctuations in the magnitude of $\bar{\psi}_6(t)$ manifest the dynamical heterogeneity in the neighborhood of the corresponding particles. It should also be noted that the timescale of the fluctuations in $\bar{\psi}_6(t)$ for these particles looks similar to that for the center particle.

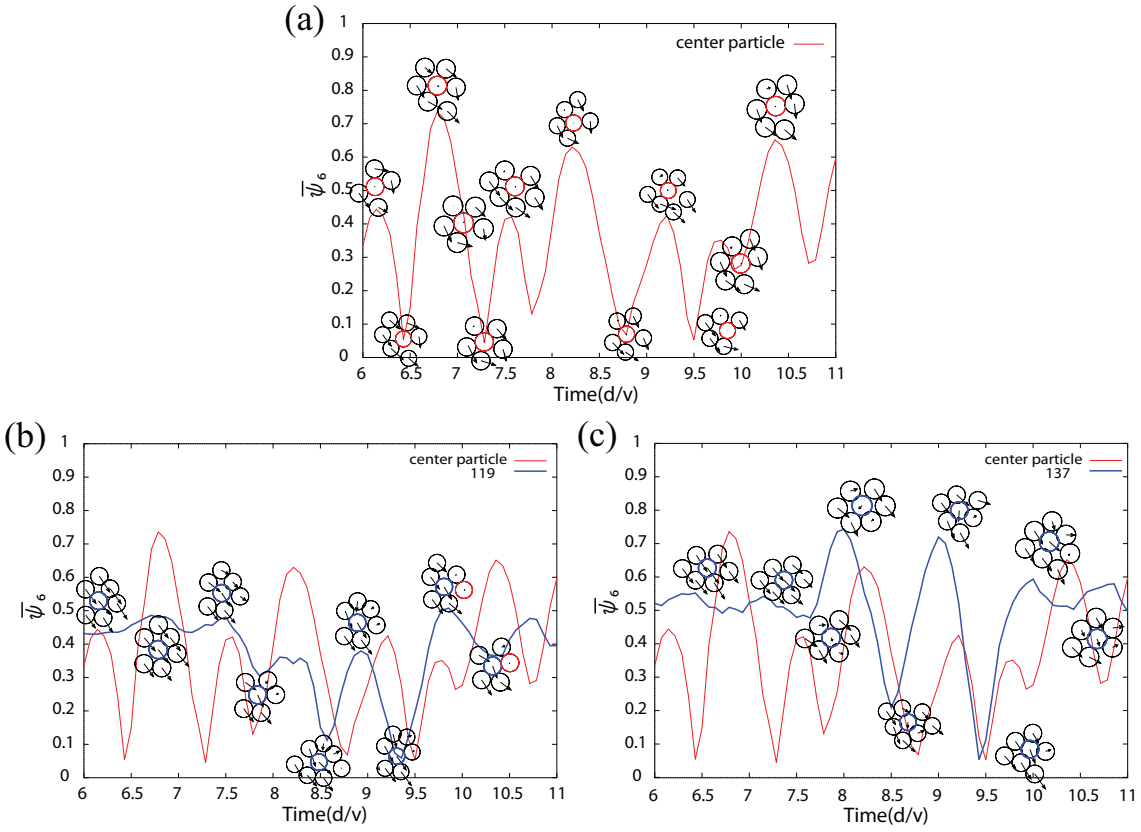

FIGURE 3.3: A series of snapshots of local configurations in the neighborhood of a particle along the time evolution associated with $\bar{\psi}_6(t)$. (a) the center particle, (b) particle 119, and (c) particle 137. The vectors indicate the displacements of the corresponding particle in time $0.5d/v$ and the center particle and particles 119 and 137 are indicated by red and blue circles, respectively. In (b) and (c) $\bar{\psi}_6(t)$ of the center particle is also shown for comparison. In (b) particle 119 undergoes direct collision to the center particle near the time 10 d/v, but in (c) particle 137 does not.

3.2 Wavelet analysis for the time series of $\bar{\psi}_6$

In order to quantitatively investigate the spatio-temporal behavior of the time variation of $\bar{\psi}_6(t)$, we employ continuous wavelet transform to $\bar{\psi}_6(t)$ and focus on the frequency component corresponding to the timescale of the perturbation by the probe particle. A set of particles that contain the frequency component appearing in a certain time duration along the time propagation can be considered as ones that respond to the perturbation. Wavelet transform analysis involves a transformation from a time series $\bar{\psi}_6(t)$ with multiplication by a window function called a wavelet function. In brief, this wavelet function operates along the time series with dilation and compression of the support of the window function, and the wavelet transform quantifies the local matching of the wavelet with the time series. If the wavelet matches well with the time series at a specific scale and location, then a large transformed value is obtained. Otherwise a small value is obtained. The transform is computed at various locations of the signal

and for various scales of the wavelet, thus filling a two dimensional time-scale plane. The continuous version of this transform is called continuous wavelet transform (CWT). It is defined as[50]

$$CWT^{\phi}_{\bar{\psi}_6}(\tau, s) = \frac{1}{\sqrt{s}} \int \bar{\psi}_6(t)\phi(\frac{t-\tau}{s})\mathrm{d}t, \tag{3.1}$$

which is a function of two variables, τ and s, the translation and scale parameters, respectively. $\phi(t)$ is called the wavelet function. Note that the scale parameter s has a reciprocal relationship with frequency f, i.e., $s = f_b/f$, where f_b is the base frequency of the wavelet function. Therefore we can rewrite Eq. 3.1 as a function of τ and f as

$$\widetilde{CWT}^{\phi}_{\bar{\psi}_6}(\tau, f) = \sqrt{\frac{f}{f_b}} \int \bar{\psi}_6(t)\phi\Big(\frac{f(t-\tau)}{f_b}\Big)\mathrm{d}t. \tag{3.2}$$

For the wavelet function, in this thesis, we choose a modified version of the Gabor wavelet defined as

$$\phi(t) = \frac{1}{\sqrt{w}}(e^{i2\pi\nu t/w} - e^{-\pi\nu^2})e^{-\pi(t/w)^2} \tag{3.3}$$

with width parameter w and frequency parameter ν. Note that, the original Gabor wavelet[51] does not contain the second term in the brackets. We have discussed the details about the modification in the Appendix B. Nevertheless, the width parameter w controls the width of the region over which $\phi(t)$ is concentrated. The smaller the value of w, the more $\phi(t)$ is confined to a smaller interval of the time axis. The value ν/w is the base frequency for the Gabor wavelet, and hence the window size depends on the value of the base frequency to be monitored. Note that there is always uncertainty between the time and frequency resolution of the window function used in the wavelet analysis: the wider (narrower) the window size, w, the better (worse) the resolution in frequency but the worse (better) the resolution in time. Several ways have been proposed to find the uncertainty bound, and the most common one is the product of the standard deviations in the time and frequency domain. Among all kinds of window functions, the Gabor wavelet is known to achieve the lowest bound of the uncertainity and obtain the best analytical resolution in the time and frequency domain[51].

In the computation, we set $\nu = 1, w = d/v$ so that the timescale of the base frequency f_b corresponds to the timescale of the perturbation applied to the probe particle, i.e., $f_b = v/d = 0.07324$/frame where $v = 0.1875\mu$m/frame is the flow velocity applied to the system and $d = 2.56 \pm 0.04\mu$m is the diameter of particles. In principle, w can be determined irrespective of any value of f_b, and, thus, as long as we increase the value of ν, the width parameter w also increases (in order to keep $f_b(= \nu/w)$ constant). This implies that we could obtain higher frequency resolution but at the same time we will lose the time resolution due to the filtering of larger w. Because of the reciprocal

relationship between scale and frequency, the value of $\nu = 1$ provides modest resolution in both frequency and time in the wavelet transform[52].

The magnitude-scalogram of the Gabor wavelet transform for the probe particle is shown in the two-dimensional time-frequency plane in Fig. 3.4 as evaluated from Eq. 3.2. Indeed, in our calculation, we varied frequencies from 0.0078 to 0.5, the Nyquist frequency. One can see that, with the above choice of ν and w, this scalogram has significant frequency components around f_b (corresponding to the yellowish bright regions). As a reminder, the bond-orientational ordering in Figs. 3.2 and 3.3(a) in the vicinity of the center particle appears and disappears repeatedly under the perturbation to the particle. From the corresponding trajectory of $\bar{\psi}_6(t)$ (Fig. 3.3(a)), the value of $\bar{\psi}_6(t)$ is relatively small < 0.5 and one particle seems to get stuck in front of the probe particle at these time regimes. Likewise, the bright regions appear roughly in an "oscillatory" manner in Fig. 3.4 and there exist some time regimes where the frequency components around f_b are absent (e.g., at time time 1, 5-6, 7.5, 9.5 d/v).

Particles whose $\widetilde{CWT}$ scalograms consist of such frequency components are expected to be involved in cage breaking and formation dynamics on some timescale when those components emerge. In order to evaluate the existence of such frequency components we calculate the power of the wavelet transform at each time t, as defined as

$$P(t) = \int_{f_b - \sigma_{f_b}}^{\text{Nyquistfrequency}} A(f,t)\mathrm{d}f, \tag{3.4}$$

where $A(f,t)$ is defined as $A(f,t) = |\widetilde{CWT}^{\phi}_{\bar{\psi}_6}(t,f)|$ and $\sigma_{f_b} \approx 0.03$ is the amount of

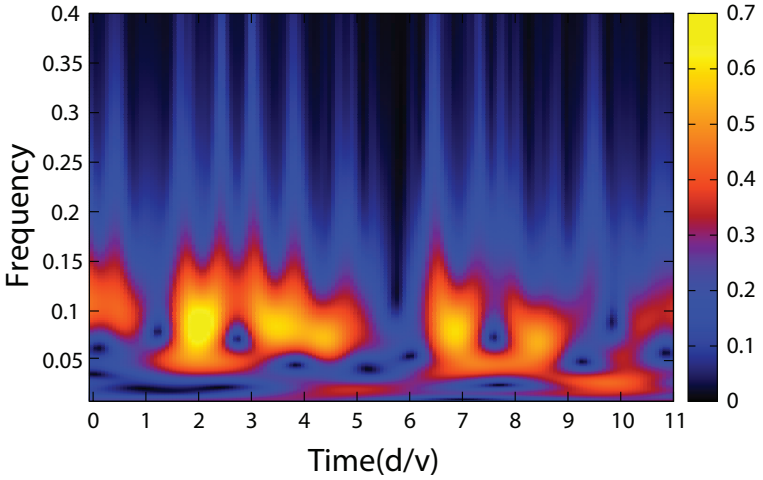

FIGURE 3.4: The $\widetilde{CWT}$ scalogram for the time series of bond-orientational structure $\bar{\psi}_6$ of the probe particle. The color bar represents the magnitude of the Gabor wavelet transform in a two-dimensional time-frequency plane.

uncertainty for the frequency component f_b. This uncertainty arises because of the finite size of the window function and can be evaluated from the Fourier transform of the Gabor wavelet[52]. Therefore the lower bound in the computation is $f_b - \sigma_{f_b}$. The upper bound is the Nyquist frequency because in the $\widetilde{CWT}$ computation we do not see any frequency component larger than 0.30.

Fig. 3.5 shows $P(t)$ for colloidal particles at some time t. One can see that particles surrounding the probe particle show relatively high power compared to particles far from the probe particle. From the time evolution of distribution of power of particles, we also notice that some particles simultaneously exhibit high power for some time duration. In fact, near that duration the bond-orientational structure around those particles are distorted and these particles are collectively involved in cage breaking and formation dynamics through the response to the perturbation. Sometimes the particles in such a high power fluctuation form in a line, sometimes they are scattered, sometimes they are in a cluster including the probe particle.

In order to look into the spatial occurrence or organization of such transient high powered particles, we plot the spatial distribution of the maximum values in the power P encountered at each position over the entire snapshots in Fig. 3.6(a). The high powered particles are mostly located in front of the center particle with a forward radial pattern that expands to the remote region from the center particle. The pattern observed here is very similar to spatial fluctuation analysis of the same data in Ref. [28]. Fig. 3.6(b) presents the spatial distribution of the averaged power P in which the average is taken over all the temporal P values of particles visiting in a space-fixed cell during the total observation time. This implies that even though some high powered particles appear in the regions remote from the probe particle they are relatively fewer and particles having high power mostly appear up to the third neighboring shell in front of the center

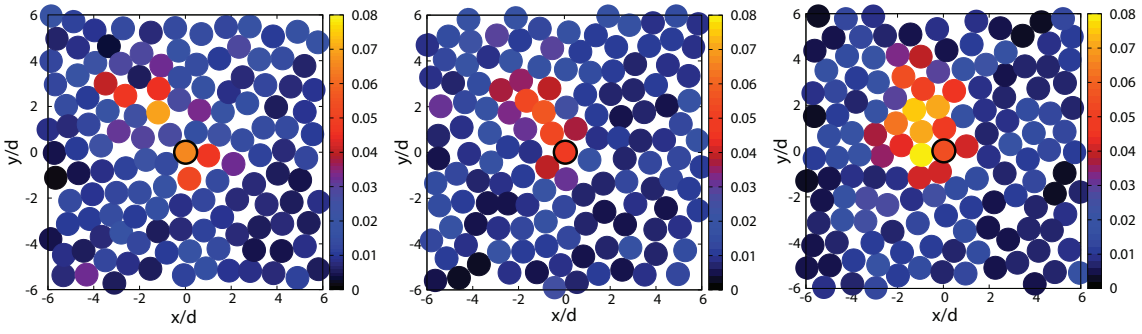

FIGURE 3.5: $P(t)$ for colloidal particles is plotted at several values of time t. The color bar represents the total power in the wavelet transform. Brighter color corresponds to higher power, therefore, contains the frequency components of interest, involving cage breaking and formation dynamics. The (optically trapped) center particle is outlined by the black circle.

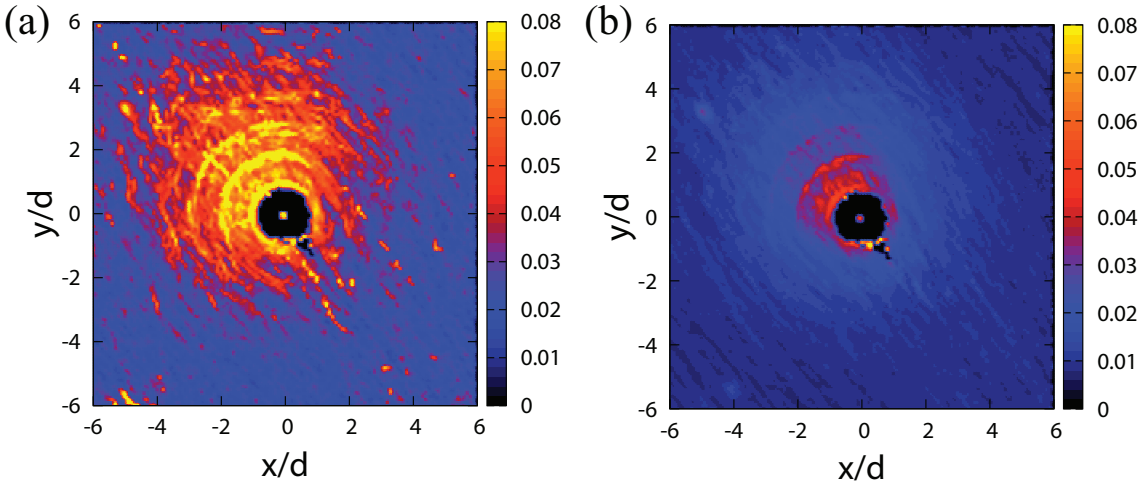

FIGURE 3.6: (a) Spatial distribution of the maximum values in the power P encountered at each position over the domain $12d \times 12d$ with the probe particle located at the center. Particles having high power are mostly located in the forepart of the probe particle. (b) Spatial distribution of the averaged power P of particles shows that high powered particles commonly occurred up to the third neighboring shell in front of the center particle. For both computations, the cell size for spatial binning is chosen as $0.15d \times 0.15d$.

particle. The results found in Fig. 3.6 shows the importance of the wavelet analysis, since such spatial pattern cannot be captured by the time averaged spatial correlation of $\bar{\psi}_6$ (Fig. C.1 in the Appendix C).

It may be obvious to have high powered particles in the first neighboring shell of the probe particle, since those particles always collide with the probe particle. However, it is far from trivial how, when, and where high powered particles emerge in the region remote from the probe particle, which result in a cage breaking and formation in that region.

3.3 FTLE/LCSs and dynamics of cage breaking and formation

In this section we analyze FTLE-based Lagrangian Coherent Structures (LCSs) to look into the dynamical foundation of the time dependent cage breaking and formation, and the question of why such spatial time-dependent organization of cage breaking and formation dynamics extends into the remote region.

3.3.1 FTLE/LCSs as separatrices

Here we consider the square domain ($12d \times 12d$) containing the probe particle at the center. For this square domain, the characteristic timescale of colloidal particles is $11d/v$. Note that choosing the integration time larger than this will make the FTLE ridges sharper and extend towards the dragging direction, i.e., top left direction. Fig. 3.7 demonstrates six consecutive snapshots of the FTLE field with the superposition of colloidal particles along the time propagation. First, one can see that the FTLE/LCSs,

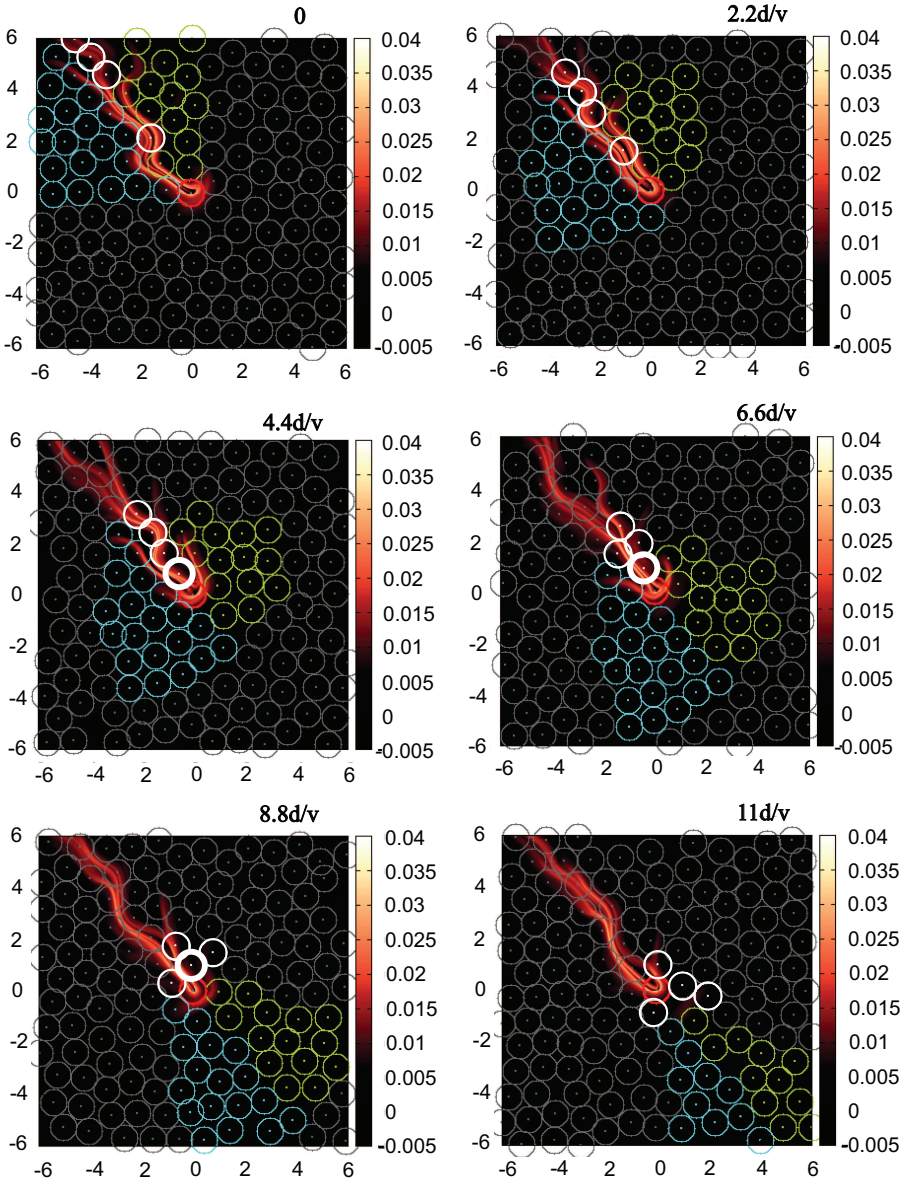

FIGURE 3.7: Time evolution of the FTLE field with the superposition of colloidal particles. At the initial time $t = 0$, green, cyan, and white particles are identified corresponding to those in the right, and left of the FTLE/LCSs, and those sandwiched by the FTLE/LCSs, respectively. See Text in section 3.3.1.

as forward FTLE ridges, exist in the forepart of the probe particle, which indicates that particles traveling and approaching to the probe particle experience some dynamical heterogeneity or frustration. In our investigation at some time instants, we have found that the most unstable directions turned out to be approximately normal to the FTLE/LCSs indicating repelling type LCSs (Fig. D.1 in the Appendix A). The most striking consequence of the application of the FTLE/LCSs is that they divide the colloidal flow into distinct regions of different dynamical characteristics. In this figure, we initially assigned a set of sample particles colored by cyan, green and white corresponding to their positions relative to the FTLE/LCSs at time $t = 0$ (the origin of time is arbitrarily chosen) and look into their advection with the time evolution of the FTLE/LCSs. Cyan and green particles are identified according to the left and right of the FTLE/LCSs, respectively, and white particles are inside the foliation of the FTLE/LCSs. The gray particles are all the rest at $t = 0$ and also particles that flow into the domain. By monitoring the time evolution of the FTLE field with the superposition of the colloid (colored) particles, one can immediately see that by the time interval $11d/v$ white particles lag while green and blue particles move forward by leaving the white particles and the probe particle. This occurs because the motions of the white particles are retarded and get caught in the surrounding FTLE ridges for some time duration when they are traveling in front of the probe particle. In particular, one white particle, outlined by a bold white circle, in the vicinity of the probe particle becomes significantly stuck from $4.4d/v$ to $8.8d/v$ and gets lagged. This affects the motion of the other white particles coming behind.

3.3.2 FTLE/LCSs break particles arrangements in colloidal fluids

From the characteristics of the FTLE/LCSs, one can expect that the presence of the FTLE/LCSs in the vicinity of a particle causes a significant distortion of the cage near the corresponding particle. It is because particles on either side of the ridges will be separated from each other, resulting in the breaking of ordered structures. Therefore, to establish a relationship between the FTLE/LCSs and the dynamics of cage breaking and formation discussed in Sec. 3.1 and 3.2, we compute the FTLE field for the integration time corresponding to the timescale of the perturbation. This timescale is the same as that used in the wavelet analysis. Fig. 3.8 shows representative samples of the FTLE field with the superposition of colloidal particles indicated by gray circles. The size of the filled white circles inside the gray circles represents their power evaluated in the wavelet transform. From the time evolution of the FTLE field superimposed the power of colloidal particles, we notice that high-powered particles are more likely located near the FTLE ridges as expected, even when the particles are located far from the center particle.

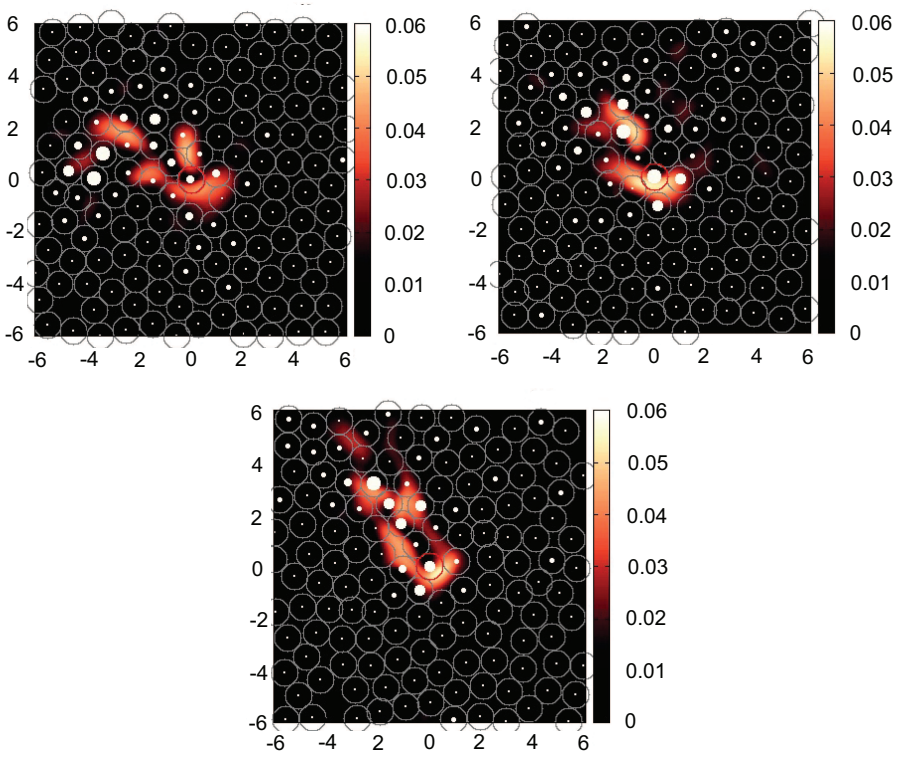

FIGURE 3.8: Samples of the FTLE field ($T = d/v$) superimposed colloidal particles (gray circle). See Text in section 3.3.2.

This result indicates that if the FTLE/LCSs penetrate the surrounding structure of high powered particles, their surrounding structure will be broken during the integration timescale, i.e., the timescale of the perturbation. In order to establish this relationship between the FTLE/LCSs and cage breaking and formation evaluated by the power in wavelet transform, we investigate the correlation between the maximum values in the FTLE field surrounding the particles and powers of the particles. Fig. 3.9 presents a 2D histogram with respect to these two quantities. The correlation coefficient is found to be 0.667 with the standard error (s.e.) ± 0.001, which tells us that the concept of FTLE/LCSs plays a pivotal role for uncovering the mechanism of cage breaking and formation dynamics.

Fig. 3.10 also shows a 2D histogram for the same quantity as in Fig. 3.9, but in this case the integration time for the FTLE field is taken for 10 times longer than that in Fig. 3.9. It is found that, for this integration time, the correlation coefficient decreases to 0.49 compared to 0.667.

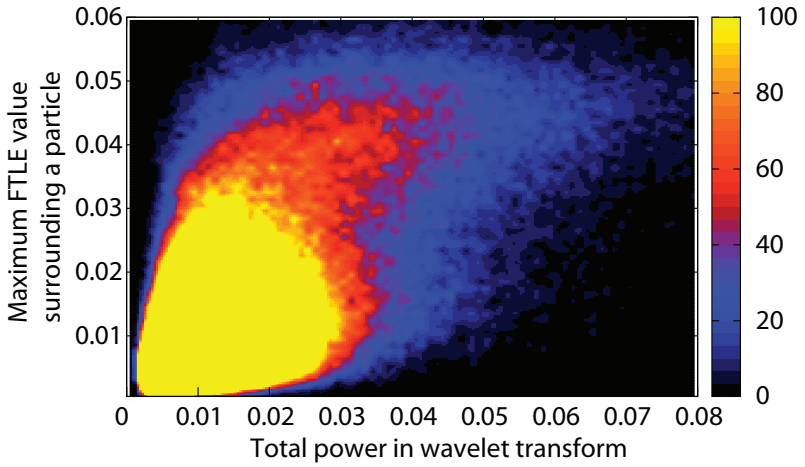

FIGURE 3.9: 2D histogram with respect to the maximum values of FTLE field surrounding individual particles and powers of the particles in the wavelet transform. The color bar gives the number of points in each bin. Large population in the plot indicates the prevalent occurrence of no cage distortion at low FTLE field in the remote region. See Text in section 3.3.2.

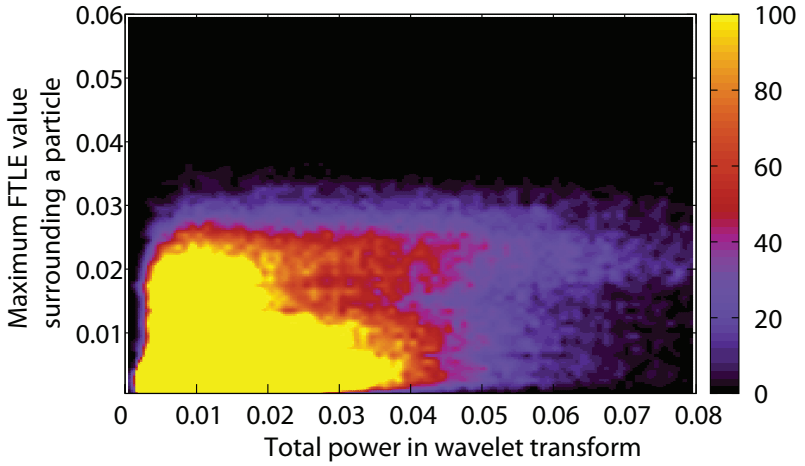

FIGURE 3.10: 2D histogram for the same quantity as in Fig. 3.9 with 10 times longer integration time than the timescale of the perturbation. The correlation coefficient is $0.490 \pm 0.001 s.e.$

Chapter 4

Conclusion and outlook

In this thesis, we have presented a modified bond-orientational order parameter $\bar{\psi}_6$ which is free from discontinuities that cause difficulties with the standard ψ_6 parameter. This modified order parameter allows us to elucidate the spatio-temporal behavior of packing distortion associated with a particle's rearrangement. The key caution is that the value of the order parameter does not necessarily reflect the behavior of the particles in ordered/disordered region for the packing fraction of the system we studied. Rather, the time variation of the $\bar{\psi}_6$ parameter does. We found that particles that undergo packing distortion on the timescale of a perturbation contain high power in the wavelet analysis. The resulting cage breaking and formation dynamics can be considered a consequence of the system's mechanical response to the perturbation, which occurs in a highly anisotropic fashion (as seen in Fig. 3.6(a)). It should be noted that high-powered particles do not necessarily mean that they have been uncaged and are actively mobile at the same time, particularly in the remote region. Indeed, the presence of "dislocated" particle pairs[43] in this region trigger a cage breaking and formation surrounding a particle even though that particle does not move actively.

We have investigated the spatial occurrence of cage breaking dynamics in terms of FTLE-based LCSs. It was shown that FTLE/LCSs can probe the spatially heterogeneous dynamics in the colloidal system. In particular, particles whose motion is highly disturbed by the perturbation can be rationalized in terms of FTLE/LCSs. In this thesis FTLE/LCSs were elucidated by the location of high amplitude in the FTLE field. However, the elucidation of characteristics of flows nearby the FTLE/LCSs is also crucial. One can intuitively think that in a system of constant dragging perturbation, the fluid parcel will be deformed in a way such that some particle will be stuck in front of the dragged particle and the nearby particles on either side will move passing through the stuck region, which may result in a sheared type deformation. However, our preliminary

investigation, as exemplified in Fig. D.1 in the Appendix A, indicates that the most stretched directions of the deformation tensor are normal to the FTLE ridges, indicating repelling type LCSs. FTLE ridges that are extracted for backward time propagation provide approximations of attracting LCSs (in forward time propagation), to which nearby particles are attracted. Such attracting LCSs can also be of great importance in understanding the formation of a free volume and trailing wake behind the probe particle under the variation of dragging speed and/or Péclet number (the ratio of the shear rate of a flow to the particle's diffusion rate).

We expect that FTLE/LCSs may be a useful tool to quantify the dynamical correlation length in spatially heterogeneous dynamics near the jamming transition, and can probe the microscopic origin of the jamming transition. Since it is difficult to investigate directly the dynamics near the density regime where the jamming transition occurs, it is vital to develop a method to extrapolate results of our analysis in the lower density regime to those near the jamming transition. To extrapolate the results from lower density regime to a higher density regime, an appropriate choice of integration time may be important. For example, in a higher density regime, deformation timescales of fluid parcels are expected to be longer as the packing fraction increases. In a lower density regime, deformation timescales can be longer or shorter depending on the Péclet number. At lower packing fraction the hydrodynamic interaction dominates particle motions instead of direct collisions among particles. Therefore, the dynamics of the particles can be different depending on the hydrodynamic interaction and the system settings. In order to investigate them, a method to determine an appropriate integration time is needed.

Another possible application of FTLE/LCSs would be for understanding the dynamical behavior of particles and phase transition associated with rheological properties, such as shear thinning, Newtonian flow and shear thickening of colloidal fluids. Application to shear thickening is expected to shed light on the lubrication hydrodynamics, formation of hydroclusters in the shear thickening regime [53, 54], and microviscosity in the field of active microrheology where the rheological properties are probed by single particle motion[27].

Question is whether the analysis that we have studied in colloidal fluids can contribute to a biological system. An experimental study within a confluent monolayer of epithelial cells[2] reports the collective migration of epithelial cells depending on the presence of their neighbors. It is found that this collective migration slows as cell density increases. This observation provide an intriguing analogy to the dynamic heterogeneity in a system composed of many particles as they become more crowded. We expect that, our analysis can provide a deep insight into the understanding of heterogeneous dynamics of different

subcellular region, and for example, collective cell migration in response to the leader cells (a sort of stimuli), in a confluent epithelial cell sheet.

Appendix A

Construction of the flow map

To construct the flow map $\mathbf{F}_{t_0}^{t_0+T}(\mathbf{x_0})$, we use instantaneous tracking of colloid particle positions from the experimental data. Here the instantaneous particle tracking results are used to estimate the small time step flow maps, $\mathbf{F}_{t_i}^{t_i+\Delta t}$, over the inter-frame time Δt. By composing a number of small time step flow maps, we are able to achieve more accurate approximation of the total flow map $\mathbf{F}_{t_0}^{t_0+T}$[42, 49], which can be written as

$$\mathbf{F}_{t_0}^{t_0+T} = \mathbf{F}_{t_0+(k-1)\Delta t}^{t_0+T} \circ \mathbf{F}_{t_0+(k-2)\Delta t}^{t_0+(k-1)\Delta t} \circ \cdots \circ \mathbf{F}_{t_0+\Delta t}^{t_0+2\Delta t} \circ \mathbf{F}_{t_0}^{t_0+\Delta t} \tag{A.1}$$

where $T = k\Delta t$ and the symbol "$\circ$" denote the function composition. Because the flow maps are needed to compute on a discrete grid of points, $\mathbf{z_0}$, an interpolation is necessary to compile them to obtain $\mathbf{F}_{t_0}^{t_0+T}$. That is, we consider a small time step flow map $\mathbf{F}_{t_i}^{t_i+\Delta t}$ and the same flow map but restricted to $\mathbf{z_0}$, i.e, $\mathbf{F}_{t_i}^{t_i+\Delta t}|_{\mathbf{z_0}}$. Applying the interpolation, $\mathcal{I}$, on the flow map $\mathbf{F}_{t_i}^{t_i+\Delta t}|_{\mathbf{z_0}}$, we obtain an interpolated flow map $\mathcal{I}\mathbf{F}_{t_i}^{t_i+\Delta t}$ that approximates $\mathbf{F}_{t_i}^{t_i+\Delta t}$. Fig. A.1 shows an illustration to construct an interpolated small time step flow maps over the time between frames at t_0 and $t_0 + \Delta t$. Evaluating small time step interpolated flow maps consecutively allows for the total flow map to be approximated. Therefore, an approximation to the total flow map in Eq. A.1 can be obtained by

$$\begin{aligned}\widetilde{\mathbf{F}}_{t_0}^{t_0+T}(\mathbf{z_0}) &= \mathcal{I}\mathbf{F}_{t_0+(k-1)\Delta t}^{t_0+k\Delta t} \circ \mathcal{I}\mathbf{F}_{t_0+(k-2)\Delta t}^{t_0+(k-1)\Delta t} \circ \cdots \circ \mathcal{I}\mathbf{F}_{t_0+\Delta t}^{t_0+2\Delta t} \circ \mathcal{I}\mathbf{F}_{t_0}^{t_0+\Delta t}(\mathbf{z_0}) \\ &\approx \mathbf{F}_{t_0}^{t_0+T}(\mathbf{z_0}).\end{aligned} \tag{A.2}$$

As the trajectories of the particles are given on a scattered position they must be interpolated onto the points coincident with the compiled flow map at a given time step. To this end, we use the radial basis function (RBF) interpolation scheme accompanied with a multiquadric function as a basis function[55].

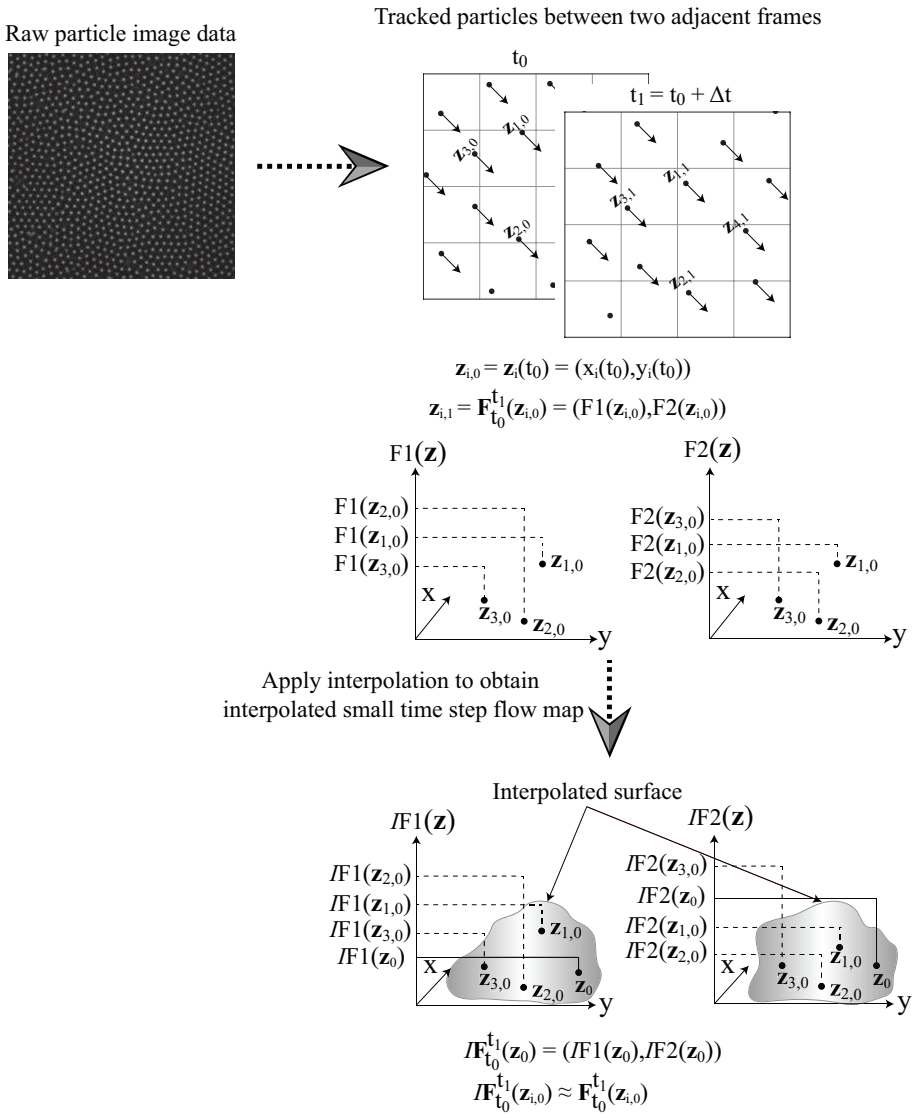

FIGURE A.1: Figure shows the construction of the interpolated small time step flow maps over two adjacent inter-frame time Δt. $\mathbf{z}_{i,j}$ is the tracking of particle i at time t_j and $\mathbf{F}_{t_0}^{t_1}$ is a small time step flow map over $[t_0, t_0 + T]$. The interpolation operator $\mathcal{I}$ acts on $\mathbf{F}_{t_0}^{t_1}$ resulting the interpolated flow map $\mathcal{I}\mathbf{F}_{t_0}^{t_1}$ which approximates $\mathbf{F}_{t_0}^{t_1}$.

Once the flow map is obtained, it is necessary to compute the Jacobian of the flow map $\mathbf{F}_{t_0}^{t_0+\Delta t}$ to obtain the Cauchy-Green deformation tensor. This Jacobian of the flow map can be obtained by applying the chain rule to Eq. A.1 resulting the product of the Jacobians of the small time step flow maps, which yields

$$\mathbf{DF}_{t_0}^{t_0+T} = \mathbf{DF}_{t_0+(k-1)\Delta t}^{t_0+T} \times \mathbf{DF}_{t_0+(k-2)\Delta t}^{t_0+(k-1)\Delta t} \times \cdots \times \mathbf{DF}_{t_0+\Delta t}^{t_0+2\Delta t} \times \mathbf{DF}_{t_0}^{t_0+\Delta t} \tag{A.3}$$

where $\mathbf{D}$ is the Jacobian.

Appendix B

Modification of the Gabor wavelet

In general, mother wavelet (denoted by $\phi(t)$) in the wavelet transform is required to satisfy the following conditions.[50]

1. The finiteness of an integral of the squared magnitude of $\phi(t)$:

$$E = \int_{-\infty}^{\infty} |\phi(t)|^2 \mathrm{d}t < \infty. \tag{B.1}$$

2. The zero mean condition:

$$\int_{-\infty}^{\infty} \phi(t) \mathrm{d}t = 0. \tag{B.2}$$

   This condition is called the admissibility condition. Unless the admissibility condition holds, the results of the wavelet transform using such mother wavelet are different with each other between two time series $x(t)$ and $x(t) + c$ (c: a constant value), that is, only the difference is the baseline of the measurement. This is unfavorable because the underlying oscillatory timescales should not depend on constant baseline of the time series.

The original version of the Gabor wavelet [51] (also referred as complex Morlet wavelet) defined by

$$\phi(t) = \frac{1}{\sqrt{w}} e^{i2\pi\nu t/w} e^{-\pi(t/w)^2} \tag{B.3}$$

(w: width parameter, ν: frequency parameter) does not satisfy the admissibility condition:

$$\int_{-\infty}^{\infty} \frac{1}{\sqrt{w}} e^{i2\pi\nu t/w} e^{-\pi(t/w)^2} \mathrm{d}t = \sqrt{w} e^{-\pi\nu^2} \neq 0. \tag{B.4}$$

In order to meet the admissibility condition the following modification is applied to Eq. B.3 [50]:

$$\widetilde{\phi}(t) = \frac{1}{\sqrt{w}}(e^{i2\pi\nu t/w} - e^{-\pi\nu^2})e^{-\pi(t/w)^2}, \tag{B.5}$$

which yields

$$\int_{-\infty}^{\infty} \frac{1}{\sqrt{w}}(e^{i2\pi\nu t/w} - e^{-\pi\nu^2})e^{-\pi(t/w)^2}\mathrm{d}t = 0. \tag{B.6}$$

The second term in the bracket of Eq. B.5 corrects for the non-zero mean of the complex sinusoid of the first term.

Appendix C

Time averaged spatial-correlation of $\bar{\psi}_6$

We have introduced the wavelet analysis in Sec. IIIB to quantify the spatio-temporal behavior of colloidal particles under the perturbation. One might wonder whether the spatial behavior elucidated in terms of wavelet analysis can be simply observed in the time averaged spatial correlation of $\bar{\psi}_6$, $g_{\bar{\psi}_6}(\mathbf{r})$. Here we show that $g_{\bar{\psi}_6}(\mathbf{r})$ does not have any significant spatial correlation. This implies that the time averaged spatial correlation cannot capture the underlying transient structure. The time averaged spatial-correlation of $\bar{\psi}_6$ is represented by

$$\begin{aligned} g_{\bar{\psi}_6}(\mathbf{r}) &= \frac{1}{T}\int \mathrm{d}t \sum_i \delta\left(\mathbf{r} - (\mathbf{r}_i(t) - \mathbf{r}_c)\right) \\ &\quad \left(\bar{\psi}_6^c(t;\mathbf{r}_c) - \langle\bar{\psi}_6^c\rangle\right)\left(\bar{\psi}_6^i(t;\mathbf{r}_i(t)) - \langle\bar{\psi}_6\rangle(\mathbf{r}_i(t))\right), \end{aligned}$$

where

$$\langle\bar{\psi}_6^c\rangle = \frac{1}{T}\int \bar{\psi}_6^c(t;\mathbf{r}_c)\mathrm{d}t,$$

$$\langle\bar{\psi}_6\rangle(\mathbf{r}) = \frac{\int \mathrm{d}t \sum_i \bar{\psi}_6^i(t;\mathbf{r}_i(t))\delta(\mathbf{r}-\mathbf{r}_i(t))}{\int \mathrm{d}t \sum_i \delta(\mathbf{r}-\mathbf{r}_i(t))},$$

and c and T denote the center particle that is optically trapped in the colloidal assembly and the entire time length, respectively. Fig. C.1(b) shows $g_{\bar{\psi}_6}(\mathbf{r})$ larger than the standard deviation of the correlation that is estimated by the usual formula $\frac{1-g_{\bar{\psi}_6}(\mathbf{r})^2}{\sqrt{T-1}}$ with $T-1$ degrees of freedom[56]. This shows that there is no significant correlation in $\bar{\psi}_6$ after averaging over the entire time T, except the center particle itself.

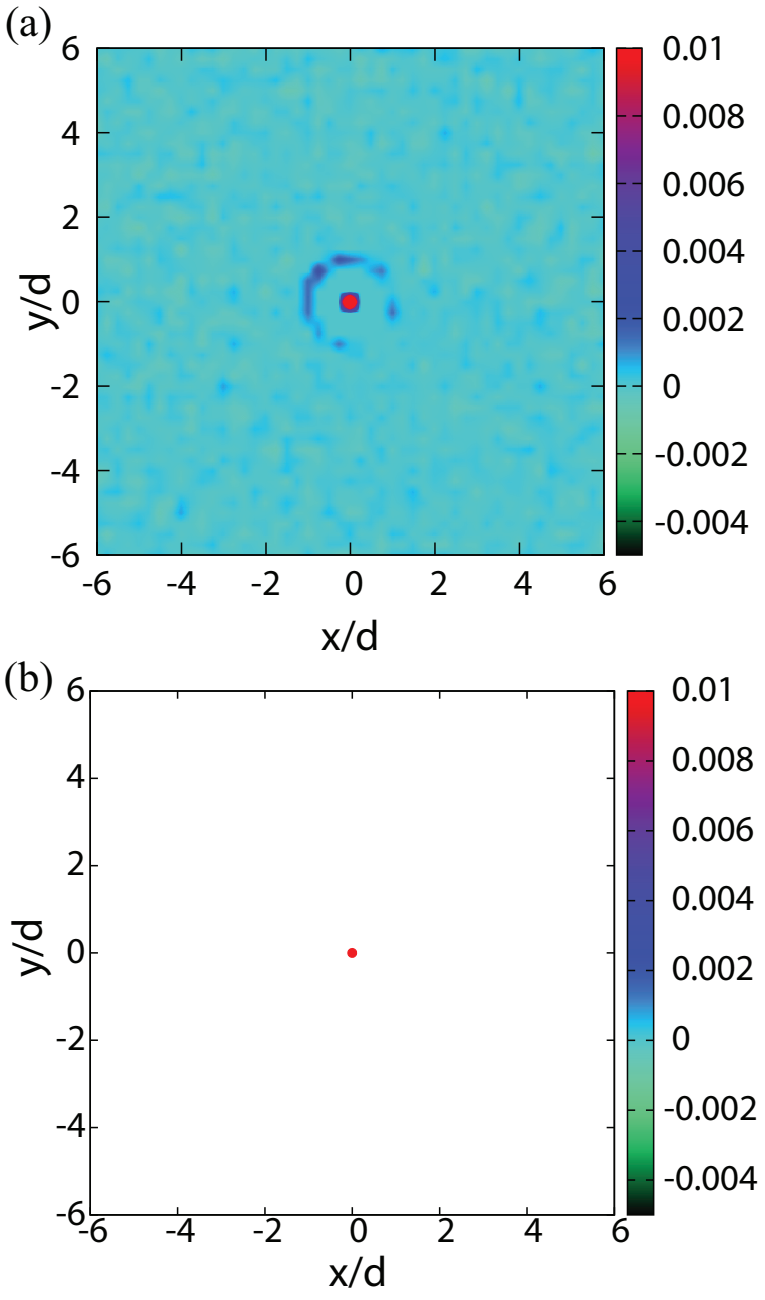

FIGURE C.1: (a)The time averaged spatial correlation of $\bar{\psi}_6$. (b) the time averaged spatial correlation of $\bar{\psi}_6$ larger than the standard error in correlation showing that the time averaged spatial correlation of $\bar{\psi}_6$ does not have a significant statistical correlation except the center particle. The color grade indicates the strength of correlation.

Appendix D

Indication of repelling LCSs

Fig. D.1 shows a representative snapshot of LCSs at a certain time instant. One can see that most of the maximal stretching directions of the deformation tensor indicated by white arrows appear normal to the FTLE ridges, indicating that these FTLE/LCSs are classified by repelling LCSs. Indeed nearby particles of the ridges are found to be repelled from each other as a response to the perturbation attributed from the center particle. Systematic analyses on the prevalence of repelling LCSs and timescale of the persistence of the LCSs will be reported elsewhere.

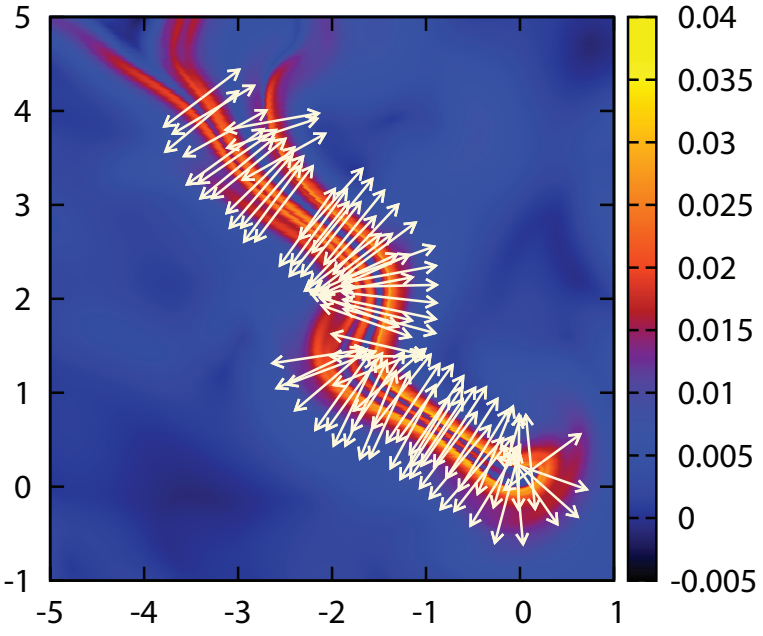

FIGURE D.1: A representative snapshot of the FTLE ridges at a certain time instant. The white arrows denote maximal stretching directions of the deformation tensor.

Bibliography

[1] Revathi Ananthakrishnan and Allen Ehrlicher. The forces behind cell movement. *International Journal of Biological Sciences*, 3(5):303–317, 2007.

[2] Thomas E. Angelini, Edouard Hannezo, Xavier Trepat, Manuel Marquez, Jeffrey J. Fredberg, and David A. Weitz. Glass-like dynamics of collective cell migration. *Proceedings of the National Academy of Sciences*, 2011. doi: 10.1073/pnas.1010059108. URL http://www.pnas.org/content/early/2011/02/09/1010059108.abstract.

[3] Willem K. Kegel and Alfons van Blaaderen. Direct observation of dynamical heterogeneities in colloidal hard-sphere suspensions. *Science*, 287(5451):290–293, 2000. doi: 10.1126/science.287.5451.290. URL http://www.sciencemag.org/content/287/5451/290.abstract.

[4] Bianxiao Cui, Binhua Lin, and Stuart A. Rice. Dynamical heterogeneity in a dense quasi-two-dimensional colloidal liquid. *The Journal of Chemical Physics*, 114(20):9142–9155, 2001. doi: http://dx.doi.org/10.1063/1.1369129. URL http://scitation.aip.org/content/aip/journal/jcp/114/20/10.1063/1.1369129.

[5] O. Pouliquen, M. Belzons, and M. Nicolas. Fluctuating particle motion during shear induced granular compaction. *Physical Review Letters*, 91:014301, Jul 2003. doi: 10.1103/PhysRevLett.91.014301. URL http://link.aps.org/doi/10.1103/PhysRevLett.91.014301.

[6] O. Dauchot, G. Marty, and G. Biroli. Dynamical heterogeneity close to the jamming transition in a sheared granular material. *Physical Review Letters*, 95:265701, Dec 2005. doi: 10.1103/PhysRevLett.95.265701. URL http://link.aps.org/doi/10.1103/PhysRevLett.95.265701.

[7] M. D. Ediger. Spatially heterogeneous dynamics in supercooled liquids. *Annual Review of Physical Chemistry*, 51(1):99–128, 2000. doi: 10.1146/annurev.physchem.51.1.99. URL http://dx.doi.org/10.1146/annurev.physchem.51.1.99.

[8] Ludovic Berthier. Dynamic heterogeneity in amorphous materials. *Physics*, 4:42, May 2011. doi: 10.1103/Physics.4.42. URL http://link.aps.org/doi/10.1103/Physics.4.42.

[9] C. A. Angell. Formation of glasses from liquids and biopolymers. *Science*, 267 (5206):1924–1935, 1995. doi: 10.1126/science.267.5206.1924. URL http://www.sciencemag.org/content/267/5206/1924.abstract.

[10] G. Marty and O. Dauchot. Subdiffusion and cage effect in a sheared granular material. *Physical Review Letters*, 94:015701, Jan 2005. doi: 10.1103/PhysRevLett.94.015701. URL http://link.aps.org/doi/10.1103/PhysRevLett.94.015701.

[11] Claudio Donati, Jack F. Douglas, Walter Kob, Steven J. Plimpton, Peter H. Poole, and Sharon C. Glotzer. Stringlike cooperative motion in a supercooled liquid. *Physical Review Letters*, 80:2338–2341, Mar 1998. doi: 10.1103/PhysRevLett.80.2338. URL http://link.aps.org/doi/10.1103/PhysRevLett.80.2338.

[12] Claudio Donati, Sharon C. Glotzer, Peter H. Poole, Walter Kob, and Steven J. Plimpton. Spatial correlations of mobility and immobility in a glass-forming lennard-jones liquid. *Physical Review E*, 60:3107–3119, Sep 1999. doi: 10.1103/PhysRevE.60.3107. URL http://link.aps.org/doi/10.1103/PhysRevE.60.3107.

[13] N. Lačević, F. W. Starr, T. B. Schrøder, and S. C. Glotzer. Spatially heterogeneous dynamics investigated via a time-dependent four-point density correlation function. *The Journal of Chemical Physics*, 119(14):7372–7387, 2003. doi: http://dx.doi.org/10.1063/1.1605094. URL http://scitation.aip.org/content/aip/journal/jcp/119/14/10.1063/1.1605094.

[14] A. R. Abate and D. J. Durian. Topological persistence and dynamical heterogeneities near jamming. *Physical Review E*, 76:021306, Aug 2007. doi: 10.1103/PhysRevE.76.021306. URL http://link.aps.org/doi/10.1103/PhysRevE.76.021306.

[15] M. E. Cates, J. P. Wittmer, J.-P. Bouchaud, and P. Claudin. Jamming, force chains, and fragile matter. *Physical Review Letters*, 81:1841–1844, Aug 1998. doi: 10.1103/PhysRevLett.81.1841. URL http://link.aps.org/doi/10.1103/PhysRevLett.81.1841.

[16] M. L. Falk and J. S. Langer. Dynamics of viscoplastic deformation in amorphous solids. *Physical Review E*, 57:7192–7205, Jun 1998. doi: 10.1103/PhysRevE.57.7192. URL http://link.aps.org/doi/10.1103/PhysRevE.57.7192.

[17] A. R. Abate and D. J. Durian. Approach to jamming in an air-fluidized granular bed. *Physical Review E*, 74:031308, Sep 2006. doi: 10.1103/PhysRevE.74.031308. URL http://link.aps.org/doi/10.1103/PhysRevE.74.031308.

[18] Aaron S. Keys, Adam R. Abate, Sharon C. Glotzer, and Douglas J. Durian. Measurement of growing dynamical length scales and prediction of the jamming transition in a granular material. *Nature Physics*, 3:260, Sep 2007. doi: 10.1038/nphys572. URL http://dx.doi.org/10.1038/nphys572.

[19] F. Lechenault, O. Dauchot, G. Biroli, and J. P. Bouchaud. Critical scaling and heterogeneous superdiffusion across the jamming/rigidity transition of a granular glass. *EPL (Europhysics Letters)*, 83(4):46003, 2008. URL http://stacks.iop.org/0295-5075/83/i=4/a=46003.

[20] Kinga A. Lorincz and Peter Schall. Visualization of displacement fields in a sheared granular system. *Soft Matter*, 6:3044–3049, 2010. doi: 10.1039/B926817K. URL http://dx.doi.org/10.1039/B926817K.

[21] R. Candelier and O. Dauchot. Creep motion of an intruder within a granular glass close to jamming. *Physical Review Letters*, 103:128001, Sep 2009. doi: 10.1103/PhysRevLett.103.128001. URL http://link.aps.org/doi/10.1103/PhysRevLett.103.128001.

[22] Raphaël Candelier and Olivier Dauchot. Journey of an intruder through the fluidization and jamming transitions of a dense granular media. *Physical Review E*, 81:011304, Jan 2010. doi: 10.1103/PhysRevE.81.011304. URL http://link.aps.org/doi/10.1103/PhysRevE.81.011304.

[23] Yuka Takehara, Sachika Fujimoto, and Ko Okumura. High-velocity drag friction in dense granular media. *EPL (Europhysics Letters)*, 92(4):44003, 2010. URL http://stacks.iop.org/0295-5075/92/i=4/a=44003.

[24] Piotr Habdas and Eric R. Weeks. Video microscopy of colloidal suspensions and colloidal crystals. *Current Opinion in Colloid and Interface Science*, 7(3–4):196 – 203, 2002. ISSN 1359-0294. doi: http://dx.doi.org/10.1016/S1359-0294(02)00049-3. URL http://www.sciencedirect.com/science/article/pii/S1359029402000493.

[25] P. Habdas, D. Schaar, A. C. Levitt, and E. R. Weeks. Forced motion of a probe particle near the colloidal glass transition. *EPL (Europhysics Letters)*, 67(3):477, 2004. URL http://stacks.iop.org/0295-5075/67/i=3/a=477.

[26] L. G. Wilson, A. W. Harrison, A. B. Schofield, J. Arlt, and W. C. K. Poon. Passive and active microrheology of hard-sphere colloids. *The Journal of Physical Chemistry*

B, 113(12):3806–3812, 2009. doi: 10.1021/jp8079028. URL http://pubs.acs.org/doi/abs/10.1021/jp8079028.

[27] Indira Sriram, Alexander Meyer, and Eric M. Furst. Active microrheology of a colloidal suspension in the direct collision limit. *Physics of Fluids*, 22(6):062003, 2010. doi: http://dx.doi.org/10.1063/1.3450319. URL http://scitation.aip.org/content/aip/journal/pof2/22/6/10.1063/1.3450319.

[28] Jelena Pesic, Joseph Zsolt Terdik, Xinliang Xu, Ye Tian, Alejandro Lopez, Stuart A. Rice, Aaron R. Dinner, and Norbert F. Scherer. Structural responses of quasi-two-dimensional colloidal fluids to excitations elicited by nonequilibrium perturbations. *Physical Review E*, 86:031403, Sep 2012. doi: 10.1103/PhysRevE.86.031403. URL http://link.aps.org/doi/10.1103/PhysRevE.86.031403.

[29] Évelyne Kolb, Jean Cviklinski, José Lanuza, Philippe Claudin, and Éric Clément. Reorganization of a dense granular assembly: The unjamming response function. *Physical Review E*, 69:031306, Mar 2004. doi: 10.1103/PhysRevE.69.031306. URL http://link.aps.org/doi/10.1103/PhysRevE.69.031306.

[30] David R. Nelson and B. I. Halperin. Dislocation-mediated melting in two dimensions. *Physical Review B*, 19:2457–2484, Mar 1979. doi: 10.1103/PhysRevB.19.2457. URL http://link.aps.org/doi/10.1103/PhysRevB.19.2457.

[31] David R. Nelson and B. I. Halperin. Solid and fluid phases in smectic layers with tilted molecules. *Physical Review B*, 21:5312–5329, Jun 1980. doi: 10.1103/PhysRevB.21.5312. URL http://link.aps.org/doi/10.1103/PhysRevB.21.5312.

[32] A. Jaster. Computer simulations of the two-dimensional melting transition using hard disks. *Physical Review E*, 59:2594–2602, Mar 1999. doi: 10.1103/PhysRevE.59.2594. URL http://link.aps.org/doi/10.1103/PhysRevE.59.2594.

[33] P. M. Reis, R. A. Ingale, and M. D. Shattuck. Crystallization of a quasi-two-dimensional granular fluid. *Physical Review Letters*, 96:258001, Jun 2006. doi: 10.1103/PhysRevLett.96.258001. URL http://link.aps.org/doi/10.1103/PhysRevLett.96.258001.

[34] Christian R. Berardi, Kipton Barros, Jack F. Douglas, and Wolfgang Losert. Direct observation of stringlike collective motion in a two-dimensional driven granular fluid. *Physical Review E*, 81:041301, Apr 2010. doi: 10.1103/PhysRevE.81.041301. URL http://link.aps.org/doi/10.1103/PhysRevE.81.041301.

[35] Keiji Watanabe and Hajime Tanaka. Direct observation of medium-range crystalline order in granular liquids near the glass transition. *Physical Review Letters*, 100:

158002, Apr 2008. doi: 10.1103/PhysRevLett.100.158002. URL http://link.aps.org/doi/10.1103/PhysRevLett.100.158002.

[36] G. Haller and G. Yuan. Lagrangian coherent structures and mixing in two-dimensional turbulence. *Physica D*, 147(3–4):352 – 370, 2000. ISSN 0167-2789. doi: http://dx.doi.org/10.1016/S0167-2789(00)00142-1. URL http://www.sciencedirect.com/science/article/pii/S0167278900001421.

[37] G. Haller. Distinguished material surfaces and coherent structures in three-dimensional fluid flows. *Physica D*, 149(4):248 – 277, 2001. ISSN 0167-2789. doi: http://dx.doi.org/10.1016/S0167-2789(00)00199-8. URL http://www.sciencedirect.com/science/article/pii/S0167278900001998.

[38] Shawn C. Shadden, Matteo Astorino, and Jean-Frédéric Gerbeau. Computational analysis of an aortic valve jet with lagrangian coherent structures. *Chaos*, 20(1): 017512, 2010. doi: http://dx.doi.org/10.1063/1.3272780. URL http://scitation.aip.org/content/aip/journal/chaos/20/1/10.1063/1.3272780.

[39] B.B. Aldridge, G. Haller, P.K. Sorger, and D.A. Lauffenburger. Direct lyapunov exponent analysis enables parametric study of transient signalling governing cell behaviour. *IEE Proceedings - Systems Biology*, 153:425–432(7), November 2006. ISSN 1741-2471. URL http://digital-library.theiet.org/content/journals/10.1049/ip-syb_20050065.

[40] Matteo Astorino, Jeroen Hamers, Shawn C. Shadden, and Jean-Frédéric Gerbeau. A robust and efficient valve model based on resistive immersed surfaces. *International Journal for Numerical Methods in Biomedical Engineering*, 28(9):937–959, 2012. ISSN 2040-7947. doi: 10.1002/cnm.2474. URL http://dx.doi.org/10.1002/cnm.2474.

[41] J. PENG and J. O. DABIRI. Transport of inertial particles by lagrangian coherent structures: application to predator–prey interaction in jellyfish feeding. *Journal of Fluid Mechanics*, 623:75–84, 3 2009. ISSN 1469-7645. doi: 10.1017/S0022112008005089. URL http://journals.cambridge.org/article_S0022112008005089.

[42] SamuelG. Raben, ShaneD. Ross, and PavlosP. Vlachos. Computation of finite-time lyapunov exponents from time-resolved particle image velocimetry data. *Experiments in Fluids*, 55(1):1–14, 2013. ISSN 0723-4864. doi: 10.1007/s00348-013-1638-8. URL http://dx.doi.org/10.1007/s00348-013-1638-8.

[43] J. S. Olafsen and J. S. Urbach. Two-dimensional melting far from equilibrium in a granular monolayer. *Physical Review Letters*, 95:098002, Aug 2005.

doi: 10.1103/PhysRevLett.95.098002. URL http://link.aps.org/doi/10.1103/PhysRevLett.95.098002.

[44] M. P. Allen and D. J. Tildesley. *Computer Simulation of Liquids*. Clarendon Press, Oxford, 1989.

[45] Thomas Peacock and John Dabiri. Introduction to focus issue: Lagrangian coherent structures. *Chaos*, 20(1):017501, 2010. doi: http://dx.doi.org/10.1063/1.3278173. URL http://scitation.aip.org/content/aip/journal/chaos/20/1/10.1063/1.3278173.

[46] Shawn C. Shadden, Francois Lekien, and Jerrold E. Marsden. Definition and properties of lagrangian coherent structures from finite-time lyapunov exponents in two-dimensional aperiodic flows. *Physica D*, 212(3–4):271 – 304, 2005. ISSN 0167-2789. doi: http://dx.doi.org/10.1016/j.physd.2005.10.007. URL http://www.sciencedirect.com/science/article/pii/S0167278905004446.

[47] George Haller and Themistoklis Sapsis. Lagrangian coherent structures and the smallest finite-time lyapunov exponent. *Chaos*, 21(2):023115, 2011. doi: http://dx.doi.org/10.1063/1.3579597. URL http://scitation.aip.org/content/aip/journal/chaos/21/2/10.1063/1.3579597.

[48] Recently, Haller(Physica D, 240, 574 (2011)) has defined LCSs rigorously in terms of hyperbolic material surfaces with extreme finite time repulsion and extraction, to avoid spurious identification of LCSs that appear due to shear or stretching.

[49] Steven L. Brunton and Clarence W. Rowley. Fast computation of finite-time lyapunov exponent fields for unsteady flows. *Chaos*, 20(1):017503, 2010. doi: http://dx.doi.org/10.1063/1.3270044. URL http://scitation.aip.org/content/aip/journal/chaos/20/1/10.1063/1.3270044.

[50] Paul S Addison. *The Illustrated Wavelet Transform Handbook*. Institute of Physics Publishing.

[51] D. Gabor. Theory of communication. part 1: The analysis of information. *The Journal of the Institution of Electrical Engineers - Part III: Radio and Communication Engineering*, 93(26):429–441, November 1946. doi: 10.1049/ji-3-2.1946.0074.

[52] The Fourier transform of the Gabor wavelet is given by $\Phi(f) = \frac{\nu}{f_b} \exp[-\pi\left(\frac{\nu(f-f_b)}{f_b}\right)^2]$ that is a Gaussian form of frequency f with mean f_b and the standard deviation $\sigma_{f_b} = \frac{1}{\sqrt{2\pi}} \frac{f_b}{\nu}$. Here σ_{f_b} provides the amount uncertainty to the identification of f_b in the frequency plane. As ν is smaller (larger), the uncertainty becomes larger (smaller) in frequency (while the uncertainty in time (scale) becomes smaller (larger)

in the wavelet transform). In our analysis, the time scale of perturbation is about 14 frames. In our study, we set two conditions to decide the value of ν: to have time resolution at least 14 frames which can be captured by choosing $\nu \leq 1$, and to distinguish the base frequency f_b to the other frequency components. In this sense, The value of ν less than 1 will increase the uncertainty in frequency which makes it difficult to differentiate the base frequency f_b from the other component. Therefore, we choose $\nu = 1$ as the optimal choice to compromise these conditions.

[53] John R. Melrose and Robin C. Ball. "contact networks" in continuously shear thickening colloids. *Journal of Rheology*, 48(5):961–978, 2004. doi: http://dx.doi.org/10.1122/1.1784784. URL http://scitation.aip.org/content/sor/journal/jor2/48/5/10.1122/1.1784784.

[54] Xiang Cheng, Jonathan H. McCoy, Jacob N. Israelachvili, and Itai Cohen. Imaging the microscopic structure of shear thinning and thickening colloidal suspensions. *Science*, 333(6047):1276–1279, 2011. doi: 10.1126/science.1207032. URL http://www.sciencemag.org/content/333/6047/1276.abstract.

[55] William T. Vetterling Brian P. Flannery William H. Press, Saul A. Teukolsky. *Numerical Recipes*. Cambridge University Press, third edition, 2007.

[56] Philip Bobko and Angela Rieck. Large sample estimators for standard errors of functions of correlation coefficients. *Applied Psychological Measurement*, 4(3):385–398, 1980. doi: 10.1177/014662168000400309. URL http://apm.sagepub.com/content/4/3/385.abstract.